Development of a Miniature, Fiber-optic Temperature Compensated Pressure Sensor

Mohammad Shah Al-Mamun

Thesis submitted to the faculty of the
Virginia Polytechnic Institute and State University
In partial fulfillment of the requirements for the degree of

Master of Science
In
Electrical Engineering

Anbo Wang, Chair
Gary R. Pickrell
Yizheng Zhu

September 17, 2014
Blacksburg, Virginia

Keywords: Fabry-Perot interferometer, White-Light Interferometry, graded index multimode fiber, silica tube, fiber-optic sensor

Development of a Miniature, Fiber-optic Temperature Compensated Pressure Sensor

Development of a Miniature, Fiber-optic Temperature Compensated Pressure Sensor

Mohammad Shah Al-Mamun

ABSTRACT

Since the invention of Laser (in 1960) and low loss optical fiber (in 1966) [1], extensive research in fiber-optic sensing technology has made it a well-defined and matured field [1]. The measurement of physical parameters (such as temperature and pressure) in extremely harsh environment is one of the most intriguing challenges of this field, and is highly valued in the automobile industry, aerospace research, industrial process monitoring, etc. [2]. Although the semiconductor based sensors can operate at around 500^{o}C, sapphire fiber sensors were demonstrated at even higher temperatures [3].

In this research, a novel sensor structure is proposed that can measure both pressure and temperature simultaneously. This work effort consists of design, fabrication, calibration, and laboratory testing of a novel structured temperature compensated pressure sensor. The aim of this research is to demonstrate an accurate temperature measurement, and pressure measurement using a composite Fabry-Perot interferometer. One interferometer measures the temperature and the other accurately measures pressure after temperature compensation using the temperature data from the first sensor.

Acknowledgements

In the first place, I would like to thank my advisor Dr. Anbo Wang for providing me the opportunity to conduct my graduate research at the Center for Photonics Technology (CPT). Dr. Wang's encouragement and guidance always motivated me to enhance my research skills throughout my entire tenure at CPT. I would also like to express my sincere gratitude to the committee members, Dr. Gary R. Pickrell and Dr. Yizheng Zhu for their continuous guidance, and support during my graduate studies.

I would like to thank my project manager Dr. Zhihao Yu for his invaluable assistance, and time to time technical discussions. Thanks to Dr. Dorothy Wang and Dr. Brian L. Scott for their excellent support and cooperation. My gratitude also goes to Zhipeng Tian, Bo Liu, Michael Fraser, Di Hu, Amiya Behera, Li Yu, Lingmei Ma Scott Zhang, and Keith Depew for their excellent cooperation. I am also thankful to my parents, family and friends for supporting me and being in my life.

Table of contents

List of figures

CHAPTER 1: Introduction

1.1 Introduction to the optical fiber

Since the very early days, people have wanted to communicate and exchange messages in a faster, reliable, and significantly cost-effective way. The very first milestone was the invention of telegraph by Samuel F. B. Morse in 1838 [4], followed by the significant research effort to guide light through the optical fiber since 1950 [5]. Corning developed the first low loss optical fiber in 1970 (losses < 20 dB/km)[6], and later they invented the high silica-core multimode fiber with losses equal to 4 dB/km [7]. Besides, the significant advancement in optoelectronics further boosted the communication through the optical fiber. The modern state of the art optical fibers (with attenuation <0.6 dB/km at 1300nm and <2.3 dB/km at 850 nm) [8] completely dominates this communication field. Different operating wavelengths have a different level of attenuation in the optical fiber. Figure 1.1.1 shows several low loss windows in the optical fiber. From the figure, it is obvious why the 1550 nm wavelength is the most preferable one for fiber-optic communication system.

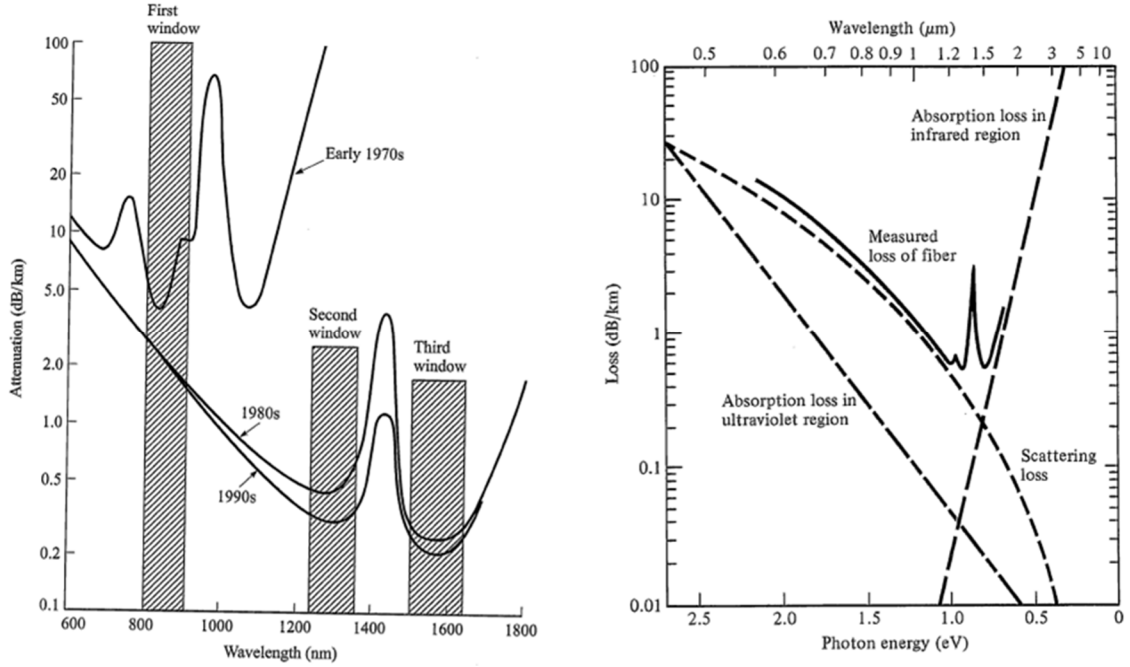

Figure 1.1.1: The attenuation of optical fiber (left), loss components (right) as a function of wavelength *[9, 10]*. Used under fair use, 2014

Again, light is an electromagnetic wave which travels at a very high speed ($c = 3x10^8$m/s) in the free-space. However, in a non-conducting medium, it travels at a reduced speed V (where $V<c$). Whether the light will travel faster or slower within a medium depends on the type of material, and can be expressed by Equation (1-1),

$$n = \frac{C}{V} \qquad (1\text{-}1)$$

where n is the refractive index of the material, and V is the speed of light in that medium. Since $V<c$,

the refractive index is always greater than 1 ($n > 1$). From Equation (1-1), it can also be concluded that as the density of a medium increases the velocity of light decreases.

1.2 Light guiding principles in the optical fiber

When light comes into an interface that has a change of refractive index, part of the light is reflected back into the incident medium, while the residuals are refracted into the second medium. The bending of light in medium 2 compared to medium 1 depends on the change of refractive indexes among those media. If light is entering from medium 1 into medium 2, Snell's law can be used to express the relationship between the angle of incidence and angle of refraction. This is shown by Equation (1-2),

$$n_1 \sin\theta_1 = n_2 \sin\theta_2 \qquad (1\text{-}2)$$

where n_1 and n_2 are the refractive indexes of medium 1 and medium 2 respectively, θ_1 is the angle of incidence (angle between the normal line and incident ray), and θ_2 is the angle of refraction (angle between the normal line and refracted ray).

Angle of incidence is also equal to the angle of reflection. The incident ray, normal to the interface, reflected ray, and refracted ray all are in the same plane. This plane is named as the plane of incidence. In accordance with Equation (1-2), it can be easily concluded that when light travels from a medium of low refractive index to a high refractive index (dense optical medium), the refracted ray gets nearer to the normal line. On the other hand, if light travels from an optically dense medium to a less dense medium, the refracted ray deviates away from the normal line. These two situations are explained by Figure 1.2.1 (left and right respectively).

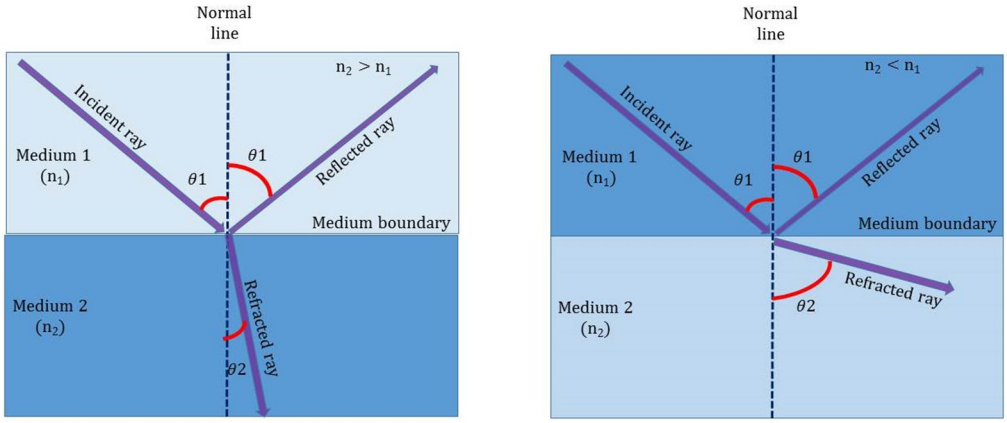

Figure 1.2.1: Refracted ray towards the normal line (left), away from the normal line (right).

Now, assuming that the incident ray is in the dense medium, and the refracted ray is in the less dense medium. If the angle of incidence (θ_1) continues to increase, the refracted ray deviates further and further from the normal line (θ_2 becomes larger). If this continues, there will be a situation when the refracted ray will be parallel to the boundary between the two media ($\theta_2 \cong 90^0$). This scenario is illustrated using Figure 1.2.2 (center). In this situation, the angle of incidence is called the critical angle ($\theta_1 = \theta_c$). If the angle of incidence increases beyond the critical angle, all the incident beams will be reflected back into medium 1, and no light will be refracted into medium 2 [11]. This phenomenon is known as the total internal reflection (TIR), and is explained by using Figure 1.2.2 (right).

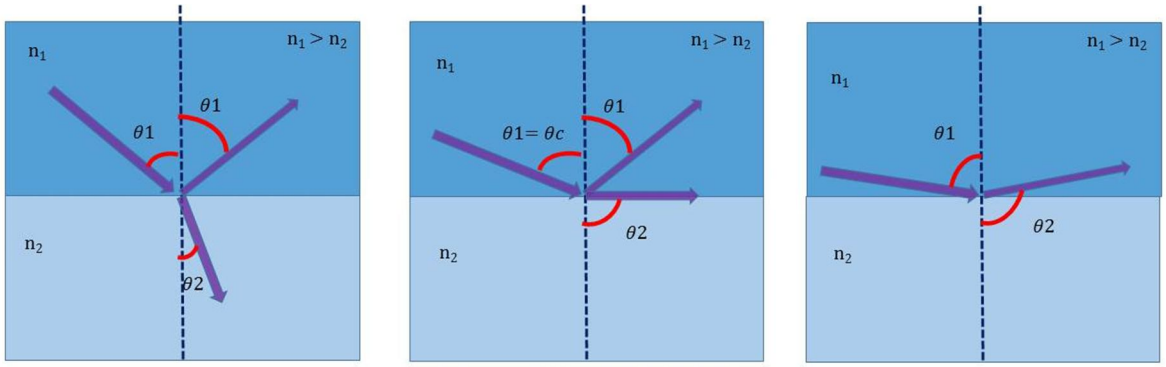

Figure 1.2.2: Total internal reflection (TIR) of the refracted ray (center & right) [11]. Used under fair use, 2014

Optical fiber is basically made of dielectric material (mainly silica), and is usually of solid cylindrical shape [11]. The inner portion usually has a higher refractive index (n_1) and is called the core. The core is surrounded by material having a slightly smaller refractive index (n_2) and is known as the cladding [11]. The cladding is then enclosed by a polymer protective coating [11]. This coating makes the fiber flexible, and prevents moisture from diffusing into the fiber materials. Light from an optical source (such as light-emitting diode or laser) is incident into one end of the fiber. But, only the beams that are incident within a certain angle (the acceptance angle), with respect to the optical axis, can be accepted by the core of the fiber. Only these beams are guided through the fiber by obeying the principle of total internal reflection [12]. Figure 1.2.3 shows the structure of a typical optical fiber.

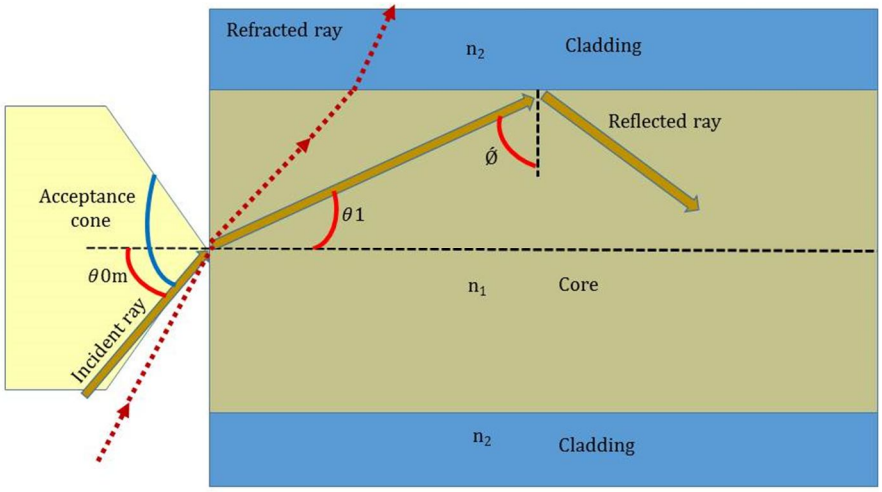

Figure 1.2.3: The guiding of light in a typical optical fiber structure *[12]*. Used under fair use, 2014

When the angle of incidence of the optical beam is beyond the acceptance angle (the red dotted line in the figure), the incident ray is no longer guided by the core of the fiber, and eventually the optical beam leaves the fiber. The measure of light that is accepted within the fiber core is denoted by a quantity called the numerical aperture (*NA*), and can be written by Equation (1-3) [12],

$$NA = n\,sin\theta_{0m} = \sqrt{n_1^2 - n_2^2} \qquad (1\text{-}3)$$

where n is the refractive index of the incident medium (usually air, and $n \cong 1$), θ_{0m} is the maximum acceptance angle, and n_1 and n_2 are the refractive indexes of the core and cladding respectively.

However, depending on the fiber structure, material and characteristics, each fiber can guide a certain number of discrete propagating modes. These guided electromagnetic waves are called the bound modes. Each of the guided modes has its own electric and magnetic field distribution, and satisfies the homogeneous wave equation based on the unique boundary condition for that specific fiber [11].

1.3 Types of optical fibers

Depending on the material composition within the fiber core, the optical fibers can be classified as: [11]

i) Step index fiber:

The core of this type of fiber has a constant refractive index. At the core-cladding interface, there is an abrupt change of refractive index. If the core has a refractive index n_1, the refractive index of the cladding abruptly changes to n_2 at the core-cladding boundary ($n_1 > n_2$).

ii) Graded index fiber:

For the graded index fiber, the refractive index of the core material is not uniform anymore. Rather, it changes gradually along the radial direction. Therefore, the fiber is named as the graded index fiber.

Again, based on the number of modes that can be guided by a fiber, the optical fibers can be classified into the following two types: [11].

i) Single mode fiber:

This type of fiber allows only one mode to propagate through its core. Since it supports only one mode, the core dimension is usually very small (typically 8~10 μm), and a high-cost optical source (such as Laser) is required to excite the single mode into the core [11].

ii) Multimode fiber:

Multimode fibers can guide multiple modes simultaneously within the core of the optical fiber. Here, the dimension of the core is much larger than that of a single mode fiber. Therefore, a low-cost optical source (such as LED) can be used to launch the optical beam into the MMF (Multimode Fiber) core. Again, each of the modes supported by the multimode fiber has a slightly different path. Therefore, each mode takes a different time to travel from one end of the fiber (optical source) to the other end (photo-detector). This leads to intermodal distortion. However, the intermodal distortion effect can be minimized by using the graded index fiber, where each mode experiences a slightly different refractive index medium along its path. Therefore, all the modes reach the photo-detector nearly at the same time. Figure 1.3.1 displays the structure of several types of optical fibers, and the corresponding propagating modes.

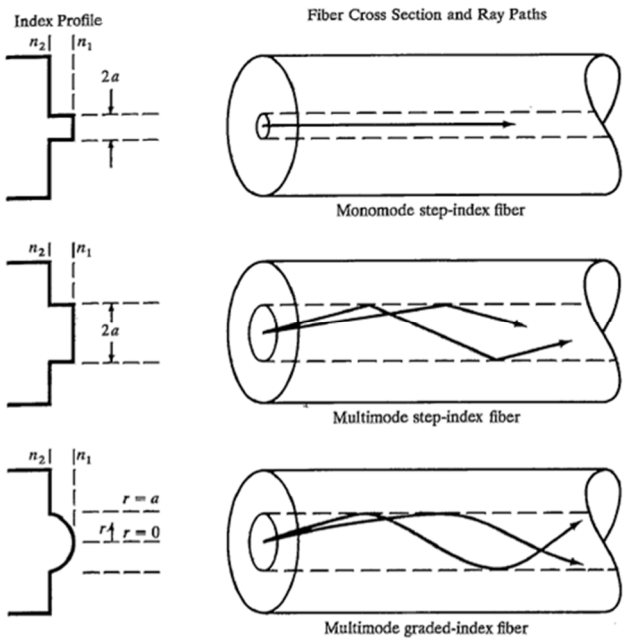

Figure 1.3.1: Typical structure of several types of optical fiber *[11].* Used under fair use, 2014

1.4 Modal concepts in optical fiber

For a mode to propagate within the optical fiber and to reach the other end of the fiber (the photo-detector), it is to be guided. A certain mode will be guided only if its propagation constant (β) satisfies the following condition [13],

$$n_2 k < \beta < n_1 k \qquad (1\text{-}4)$$

where $k = \frac{2\pi}{\lambda}$.

There is a dimensionless quantity called the *V* number, which determines whether a particular mode will be guided or not by a specific fiber. The *V* number can be defined by Equation (1-5) [13],

$$V = \frac{2\pi a}{\lambda}\sqrt{n_1^2 - n_2^2} = \frac{2\pi a}{\lambda} * NA \qquad (1\text{-}5)$$

where a is the radius of the fiber core, λ is the wavelength of the incident optical beam in vacuum, and *NA* is the numerical aperture.

The *V* number depends on the fiber geometry (core radius) and the refractive index of the core and cladding. For a specific mode to exist in a fiber, the *V* number of that fiber has to exceed a certain minimum value. In other words, every mode has a different *V* limit, and a particular mode is cutoff (does not exist or is not guided) when $\beta = n_2 k$. This happens when $V \leq 2.405$. The lowest order mode, HE_{11}, has no cutoff, and is always guided [13]. In this case, only one mode exists, and the fiber is single mode. Figure 1.4.1 indicates several lower order modes and the corresponding propagation constants as a function of *V* number. Once a mode satisfies the minimum V limit, that particular mode is then guided by the fiber.

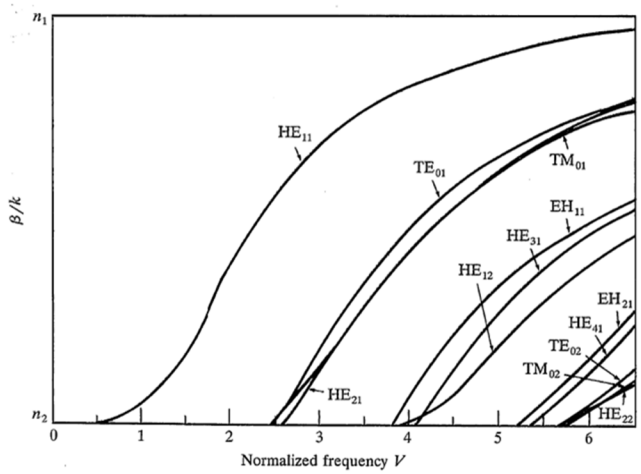

Figure 1.4.1: The propagation constant as a function of *V* number for some lower order modes *[14]*. Used under fair use, 2014

Again, for a large *V* number, the total number of modes that can exist in a multimode fiber can be estimated by Equation (1-6) [13].

$$M \approx \frac{1}{2}\left(\frac{2\pi a}{\lambda}\right)^2\sqrt{n_1^2 - n_2^2} = \frac{V^2}{2} \qquad (1\text{-}6)$$

1.5 Fiber-optic sensors

Significant research and development efforts are underway in fiber-optic sensor technology for the last four decades [1, 15]. Fiber-optic sensors are made of insulating materials, unaffected by any electromagnetic interference, and highly suitable for extremely corrosive and harsh environment [16].

The fundamental components of a typical fiber-optic sensor are an optical source (LED or Laser), a transducer (single mode or multimode fiber, etc.) and a receiver (a photo-detector to detect the modulated signal by the environmental disturbance of interest) [15, 17]. Figure 1.5.1 shows the schematic of a typical fiber-optic sensor system.

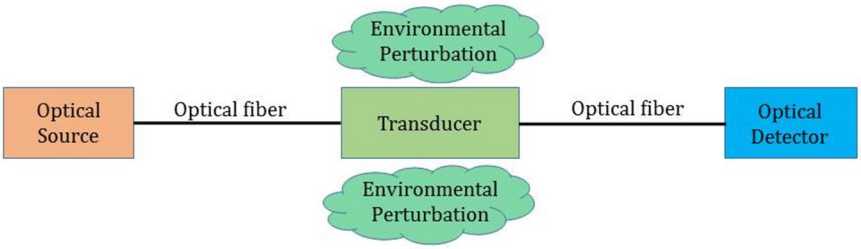

Figure 1.5.1: Schematic of a fiber-optic sensor system *[15]*. Used under fair use, 2014

Amplitude, frequency, state of polarization, phase, etc. [17] are some of the optical parameters that are usually modulated by the environmental effects in an fiber-optic sensor system. The basic components of this system are also listed in Figure 1.5.2.

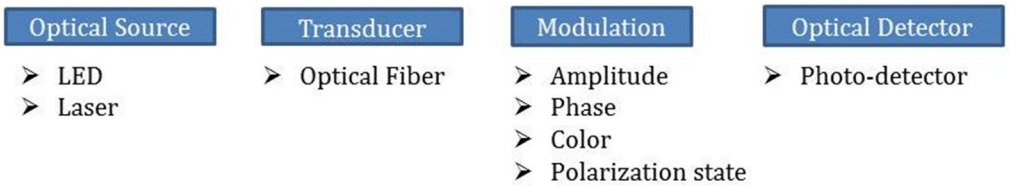

Figure 1.5.2: Fundamental components of a fiber-optic sensor system *[17]*. Used under fair use, 2014

1.6 Advantages of fiber-optic sensors

The current state of the art fiber-optic sensors have numerous applications in diverse technological fields, and they can monitor wide range of environmental quantities such as strain, rotation, vibration, light intensity, color, flow, temperature, pressure, chemically induced changes, refractive index, liquid level, acceleration, displacement, electric field, current, magnetic field, etc. Fiber-optic sensors have significant advantages over traditional sensors, such as: [16, 18]

i) Fiber-optic sensors are very small in size, light in weight, free from fire hazard, and can be used to sense usually inaccessible tiny segments without affecting the sensor signal.

ii) The fiber-optic sensor signal is immune to electromagnetic interference (EMI) and ionizing radiation; therefore it eliminates the need to use any interference immunity shielding.

iii) These sensors have high sensitivity and high accuracy.

iv) Fiber-optic sensors are chemically inactive and therefore can be used as chemical or biomedical sensors. They can also measure pressure and temperature in extremely harsh and corrosive environment.

v) With the aid of optoelectronics and low loss optical fiber, the fiber-optic sensors can be used for remote-sensing applications.

vi) By exploiting the huge bandwidth of the optical fiber, a large number of fiber-optic sensors can be multiplexed along the single fiber to realize the distributed fiber-optic sensing.

1.7 Types of fiber-optic sensors

There are many ways to classify the fiber-optic sensors. Based on the sensing locations, fiber-optic sensors can be classified as: [15, 16]

i) Extrinsic fiber-optic sensors

ii) Intrinsic fiber-optic sensors

i) Extrinsic fiber-optic sensors

In extrinsic fiber-optic sensors, the interferometric cavity is not within the fiber. So, the optical beam has to leave the fiber to reach the sensing region. In the sensing region, the environmental perturbation modulates the intensity, phase, or frequency of the optical beam. The modulated beams are reflected back towards the detector, form an interference pattern, and are detected by the detector. These types of sensors are also called as hybrid fiber-optic sensors [15].

Figure 1.7.1 shows the schematic of a classic extrinsic fiber-optic sensor [19]. The light carried by the SMF (single mode fiber) comes into the silica tube. Environmental variation of interest changes the optical beam within the tube. A fraction of the optical beam is reflected back from each of the SMF/silica tube interfaces. In this structure, there are two such reflected beams, which are forwarded towards the detector through the lead-in fiber. All the reflected beams combine to constitute an interference pattern, which is detected by the photo-detector. After the detection and demodulation, the environmental variation can be measured.

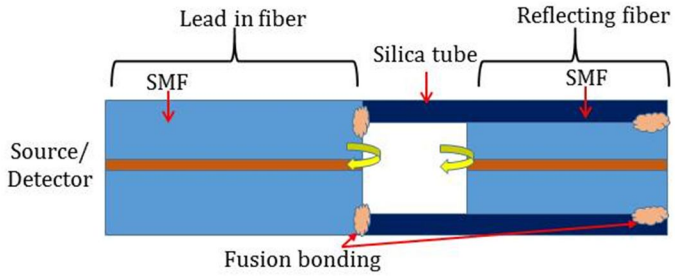

Figure 1.7.1: Schematic of a classic extrinsic fiber-optic sensor *[19]*. Used under fair use, 2014

ii) Intrinsic fiber-optic sensors

For this type of sensor, the environmental effect modulates the intensity, phase, frequency, or polarization, etc. of the optical beam, while the light propagates within the core of the optical fiber [15]. The modulated optical beam is then reflected back towards the detector. Therefore, the interferometric cavity is within the fiber, and the light never leaves the fiber throughout the sensing process. Intrinsic fiber-optic sensor has a high resolution and sensitivity, which is used to measure pressure, temperature, strain, etc. [15]. These sensors are also known as all-fiber sensors.

Figure 1.7.2 shows the structure of a typical intrinsic fiber-optic sensor. A segment of MMF (multimode fiber) is spliced between the two SMFs (single mode fibers). There is a reflection from each of the SMF/MMF interfaces. The interference pattern formed by the reflected beams can be detected by the photo-detector.

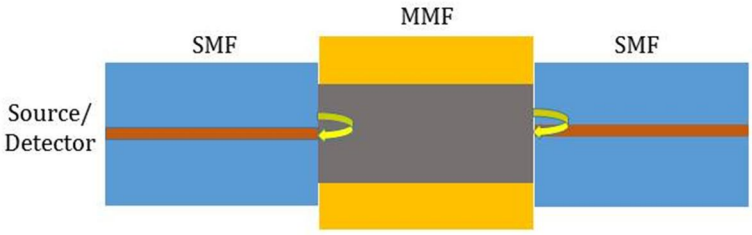

Figure 1.7.2: Schematic of a typical intrinsic fiber-optic sensor *[20]*. Used under fair use, 2014

Moreover, according to the types of optical modulation scheme, the fiber-optic sensors can be classified as the following three types: [16]

iii) Intensity modulated fiber-optic sensors

iv) Wavelength modulated fiber-optic sensors

v) Phase modulated fiber-optic sensors

iii) Intensity modulated fiber-optic sensors

This type of fiber-optic sensor is based on the principle of intensity modulation. If environmental factors modulate the optical beam intensity, the factors can be estimated by measuring the change of intensity. There are numerous examples of intensity based fiber-optic sensors [15]. Two of them are discussed here:

Figure 1.7.3 demonstrates an example of intensity modulated fiber-optic sensor. When the guided light comes at the end of the fiber, it leaves the fiber at a certain angle with respect to the fiber axis. If a movable reflector is placed very close to the fiber end, part of the departing light is reflected back into the fiber, and eventually reaches the photo-detector. The intensity of the reflected light that is coupled back into the fiber depends on the relative distance between the fiber end and the movable reflector. If this distance increases, the amount of departed beam that is reflected back into the fiber will decrease. The received light intensity will also decrease accordingly. By measuring the change of intensity, the external effects (such as force) that move the moveable reflector can be computed [21]. Figure 1.7.3 illustrates this case, where the relative distance between the fiber end and the reflector increases from Figure 1.7.3(a) through b to c sequentially. The corresponding reflected beam intensity diminishes accordingly.

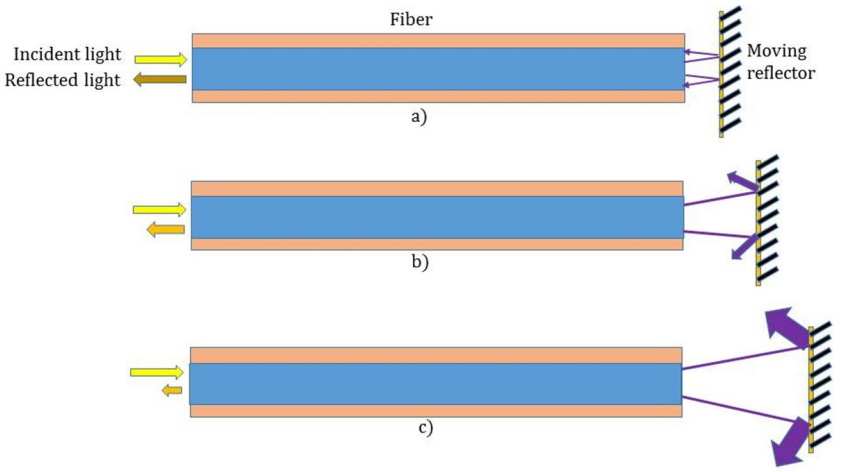

Figure 1.7.3: Conceptual schematic of an intensity modulated fiber-optic sensor *[21]*. Used under fair use, 2014

Figure 1.7.4 illustrates another type of intensity modulated fiber-optic sensor, micro-bend pressure sensor. If an external perturbation (such as pressure, vibration, etc.) is applied to the fiber, the corresponding fiber lengths will bend. Therefore, some light will be leaked out of the fiber, and the received light intensity will decrease accordingly. By measuring the change of the received beam intensity, the applied perturbation can be measured [22]. However, the intensity modulated sensors are simple, and have straightforward signal interpretation and multiplexing capability. But they have several drawbacks, such as source intensity fluctuation, low sensitivity, fiber bending loss, etc. [22]. The intensity based sensors are not widely used.

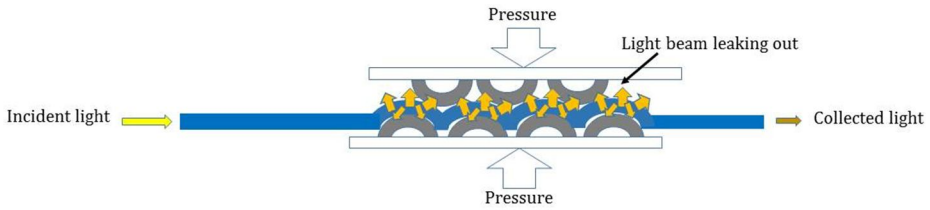

Figure 1.7.4: Schematic of an intensity modulated fiber-optic sensor *[22]*. Used under fair use, 2014

iv) Wavelength modulated fiber-optic sensors

The basic principle of this type of sensor is the modulation of optical beam wavelength by the environmental effects to be measured. FBG (Fiber Bragg Grating), phosphorescence, blackbody radiations, etc. are some of the examples of wavelength modulated sensors [15].

Figure 1.7.5 shows the schematic of a typical blackbody radiation sensor [15]. Usually, the blackbody-cavity stays at the end of the fiber and is heated. As the temperature increases, the blackbody-cavity radiates like an optical source. The radiated optical beam propagates down the fiber and reaches the detector end. Finally, the radiation profile can be detected by using a composite system of detector, lens, and filter. This radiation profile can then be used to measure the temperature. The blackbody radiation sensor works accurately at higher temperatures, but at lower temperatures, it suffers from low SNR (Signal to Noise Ratio) [15].

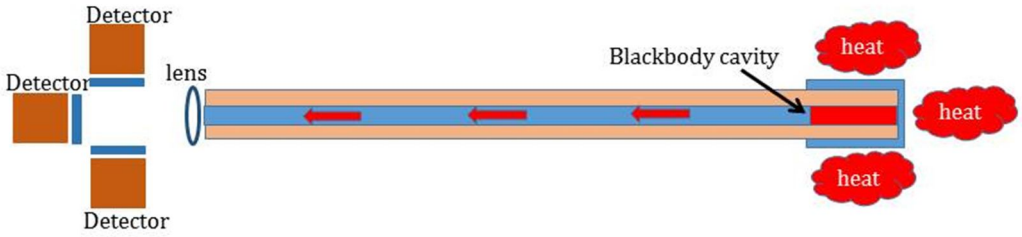

Figure 1.7.5: Schematic of a typical blackbody radiation sensor *[15]*. Used under fair use, 2014

v) Phase modulated fiber-optic sensors

The phase difference between the two optical beams can be modulated by the environmental effects, which are generally detected by using the combination of coherent optical source and interferometry techniques [15]. Although there are various configurations of phase modulated sensors, Fabry-Perot (FP) interferometer is discussed here because of its high resolution and sensitivity [23].

Fabry-Perot (FP) interferometer based sensors usually consist of two partially reflective mirrors [15]. All the reflected beams from the mirrors combine, and create an interference pattern. Depending on the level of reflection, Fabry-Perot interferometer can be either in transmission mode (when the reflection from the mirror is high), or reflection mode (when the reflection is low) [23]. A typical Fabry-Perot interferometer is shown in Figure 1.7.6 [24]. In this structure, there are two partially reflective mirrors, each mirror at the single mode fiber/air bubble interface. The distance between the two air bubbles is the cavity length. When, the environmental effects (such as pressure, temperature, strain, etc.) modulate the cavity length, the phase difference between the reflected beams changes. Therefore, by measuring the variation of phase difference, the environmental effects can be estimated [15]. The Fabry-Perot (FP) interferometric sensor has

an enormous potential for quasi-distributed sensing, which does not require any additional optical components, and is extensively used in many applications [25].

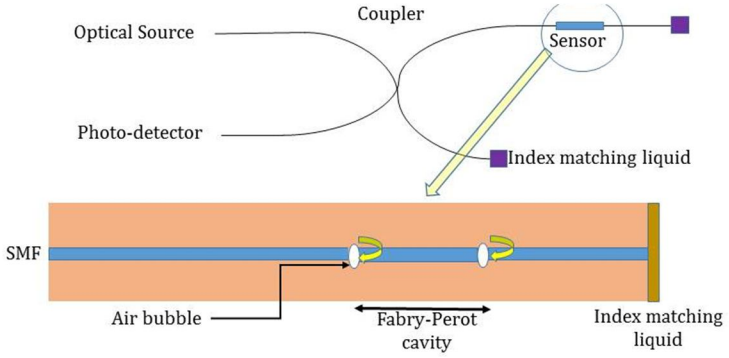

Figure 1.7.6: Schematic of a typical IFPI sensor *[24]*. Used under fair use, 2014

There are many types of interferometers, such as: [26]

i) Sagnac interferometer

ii) Ring resonator

iii) Mach-Zehnder interferometer

iv) Michelson interferometer

v) Dual mode interferometer

vi) Polarimetric interferometer

vi) Grating based interferometer

vii) Etalon based interferometer, etc.

1.8 Background of the proposed research

A pressure sensor that can operate accurately in a high-temperature environment is very lucrative in many industries, such as automobiles, power plants, turbine engines, material processing, etc. [2]. However, if the temperature is increased as high as 500^{o}C or beyond, it will impose great technological challenges on the material selection, design, packaging, long-term durability, and reliability of the sensor [27].

Traditional semiconductor based pressure sensors are generally diaphragm based which are either piezoresistive, or capacitive [2]. Piezoresistive silicon-on-insulator (SOI) pressure sensors were demonstrated by several research groups. Shuwen Guo et al. confirmed the SOI pressure sensor with operating range of 16~ 600psi and 25~500^{o}C [28]. Anthony D. Kurtz et al. reported the piezoresistive based sensors which can operate at temperature 25~480°C and pressure 14~150psi [29]. Later, the researcher also reported sensors based on the SOI with operating range of 5~1000psi and 25~600^{o}C [30]. However, the SOI pressure sensors are based on the silicon carbide (SiC), and are usually limited to 500^{o}C [31].

Yizheng Zhu et al. successfully demonstrated the high-temperature operation of an all-silica based fiber tip pressure sensor at operable pressure and temperature of 15~30psi & 24~611^{o}C and 20~160psi & 24~710^{o}C by using a thin and thick diaphragm respectively [2]. Diaphragm based all-silica pressure sensor was also confirmed by Xingwei Wang et al. which can operate up to 600^{o}C and 100psi [32]. Single mode fiber and photonic crystal fiber based Fabry–Perot interferometer with operating range of 0–5802psi and 25~700°C was reported by Chuang Wu et al. [33].

However, one of the major challenges of high-temperature operation of pressure sensor is the selection of materials. In semiconductor based sensors, various types of materials (such as silicon, pyrex, etc.) are usually used during the sensor fabrication process [2]. Different materials have different coefficient of thermal expansion (CTE), and therefore could lead to the development of stress and potential failure of the sensor structure. This effect is more pronounced at elevated temperatures. If the low-temperature materials (such as polymer epoxy, etc.) are used as the sensor materials, they will also limit the maximum operable temperature. Besides, silicon is the most common material for semiconductor based sensors, and it starts to creep at or beyond 500^{o}C [29]. This is a common problem for all the semiconductor sensors, [29] but additional cooling mechanism is not an optimum solution. On the other hand, there are several fiber-optic pressure sensors that can operate at higher temperatures [2], [32],[33]. However, most of them are diaphragm-based, and use a bonding technique to attach the diaphragm with the sensor structure [34-36]. The bonding of fused silica is exceedingly challenging, since it has a very high softening point [37]. In this thesis, an all-silica based novel fiber-optic pressure sensor is proposed that can operate at elevated temperatures. In the proposed composite sensor structure, one sensor measures the temperature (GIMM fiber cavity), and the other measures pressure (silica tube cavity) after temperature compensation using the temperature from the first sensor.

1.9 Organization of the thesis

In Chapter 1, the fundamentals of fiber optics and fiber-optic sensors are discussed. The principles of Fabry-Perot interferometer, the proposed sensor structure, and the theoretical analysis of the sensor signal are analyzed in detail in Chapter 2. Chapter 3 describes several micromachining techniques, and the step-by-step fabrication procedures to fabricate the proposed sensor structure. Once fabricated, the sensor is tested in the laboratory environment. The corresponding temperature measurement, temperature compensation mechanism, and the pressure measurement are experimentally demonstrated in Chapter 4. Finally, the potential future advances are outlined in Chapter 5.

CHAPTER 2: Theoretical background of the sensor

2.1 White-Light Interferometry system

A typical White-Light Interferometry system usually contains an optical source (LED, or semiconductor laser, or fiber laser, etc.), an optical interferometer (Michelson, or Mach-Zehnder, or Fabry-Perot, etc.), and a photo-detector to detect the sensor spectrum [38]. This interferometry based fiber-optic sensor consists of multiple reflections, where each reflection comes from a boundary between the two different refractive index materials. The reflected beams combine, constitute an interferometry signal, and are detected by the photo-detector. This type of fiber-optic sensor has high resolution, and can cover wide dynamic ranges [1]. Since this research adopts the White-Light Interferometry system, the basic principles of the system are discussed here.

2.1.1 Principle of the White-Light Interferometry

The schematic of a typical White-Light interferometry system is shown in Figure 2.1.1.

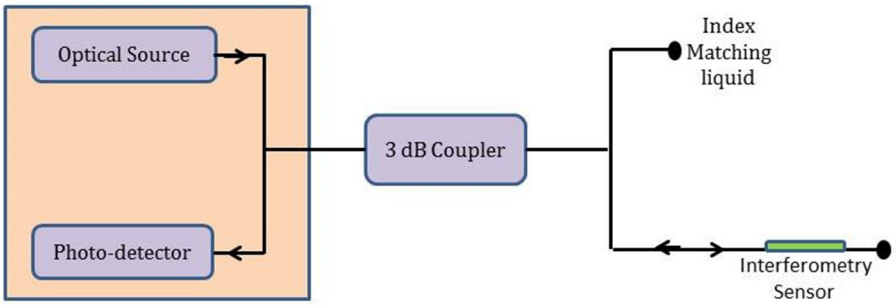

Figure 2.1.1: Schematic of a typical White-Light Interferometry system *[38]*. Used under fair use, 2014

Light originates from an optical source, passes through a 3dB directional coupler, and finally comes into the fiber-optic sensor. Within the sensor, the environmental perturbation of interest modulates the amplitude, phase, frequency, or polarization of the optical beam. The modulated beam is then reflected back by the sensor, and advances towards the photo-detector through the 3dB directional coupler. After the demodulation and processing of the reflected beam, the physical variation of interest can be quantified. The back reflection from the other end of 3 dB coupler is minimized by using an index matching liquid. However, it is a common trend to integrate the optical source (such as LED, Laser) and the optical detector (such as photo-detector) in a single module. The Micron optics SM125 Optical Sensing Interrogator used here is such an integrated system.

2.2 Fabry-Perot interferometry

The schematic of a typical Fabry-Perot interferometer is shown in Figure 2.2.1. It can be noticed from Figure 2.2.1 that the two reflective interfaces (interface 1 and interface 2) are separated by a cavity length L_1. Assuming that R_1 and R_2 are the reflectance of interface 1 and interface 2 respectively, and n is the refractive index of the material between them.

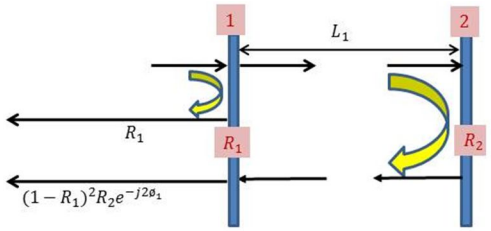

Figure 2.2.1: Schematic of a typical Fabry-Perot Interferometry system *[39]*. Used under fair use, 2014

Now if the light travels a distance L_1, the corresponding phase change $(\emptyset)$ can be expressed by Equation 2-1 [39],

$$\emptyset = \frac{(2\Pi)(2nL_1)\cos i}{\lambda} \qquad (2\text{-}1)$$

where L_1 is the cavity length, λ is the wavelength of the optical beam, and i is the incident angle and is considered as 0^o (normal incidence) for simplicity.

The normalized energy of a reflected ray can be expressed as follows: [39].

$$E_1 = R_1 + (1-R_1)^2 * R_2 e^{-j2\emptyset_1}$$

And, the complex conjugate of this ray is,

$$E_1^* = R_1 + (1-R_1)^2 * R_2 e^{+j2\emptyset_1}$$

Now, the normalized intensity can be written as, [39]

$$I = E \times E^*$$

Therefore, $I \propto \cos(\frac{4\Pi nL_1}{\lambda})$ (2-2)

It is obvious from Equation (2-2), that the reflected signal intensity is modulated by the cosine function of the Fabry-Perot cavity length (L_1). The signal intensity will be maximum or minimum when the reflections are in phase, or out of phase respectively. If the environmental perturbation changes, the cavity length (L_1) changes, and the corresponding signal intensity (I) modulates accordingly. By measuring the variation of intensity, the environmental perturbation can be quantified. The comprehensive analysis of the interferometry signals for the proposed sensor is included later in this chapter.

2.3 Fresnel's equations for reflection and refraction

The propagation of an electromagnetic wave (such as light) travelling along the z direction can be expressed as:

$$\vec{E} = \overrightarrow{E_0}\, e^{j(kz-\omega t)} \qquad (2\text{-}3)$$

where $\overrightarrow{E_0}$, k *and* ω are a complex amplitude vector, wave number, and frequency respectively.

It is well known that any plane wave is a combination of two orthogonal linearly polarized waves, one wave is parallel, and the other is perpendicular to the plane of incidence. Assuming that an optical beam is incident at medium 1 (having refractive index n_1) with an angle θ_i. Part of this beam is reflected back into medium 1 with a reflectance angle θ_r, and the remaining light is transmitted into medium 2

(having refractive index n_2) with an angle θ_t.There are two possible scenarios for this phenomenon. In one case, the electric field is parallel to the plane of incidence and is explained by Figure 2.3.1 (left). For the other case, it is perpendicular to the plane of incidence and is shown by Figure 2.3.1 (right) [40]. The objective of this analysis is to estimate the total amount of light reflected, and transmitted by the interface between the two media.

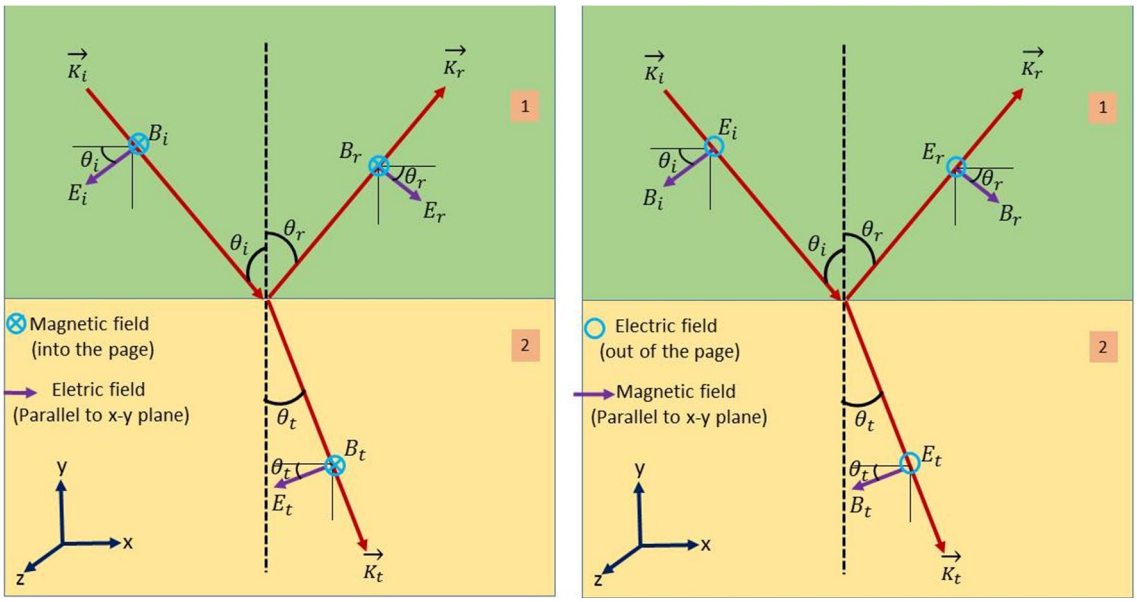

Figure 2.3.1: Schematic of: parallel polarization (left), perpendicular polarization (right) of light *[40]*. Used under fair use, 2014

However, the perpendicular polarization of the electric field (Figure 2.3.1 right) will be considered for this analysis. It is known that at the boundary between two materials, the tangential components of the electric and magnetic fields are continuous. If the electric field is along the *z* direction (*x*-*z* plane) then [40],

$$E_i(x,z,t) + E_r(x,z,t) = E_t(x,z,t) \qquad (2\text{-}4)$$

Again, if the magnetic fields are in the *x*-*y* plane and only the *x* component is considered [40],

$$-\frac{B_{ix}}{\mu_1}\cos\theta_i + \frac{B_{rx}}{\mu_1}\cos\theta_r = -\frac{B_{tx}}{\mu_2}\cos\theta_t \qquad (2\text{-}5)$$

According to the law of reflection, $\theta_i = \theta_r$, and assuming that the dielectric material is nonmagnetic,

$$\mu_i = \mu_t \cong \mu_o.$$

By keeping the complex amplitudes and getting rid of the quickly changing terms, Equation (2-4) and (2-5) can be rewritten as Equation (2-6) and (2-7) respectively.

$$E_{oi} + E_{or} = E_{ot} \qquad (2\text{-}6)$$

$$-B_{oi}\cos\theta_i + B_{or}\cos\theta_r = -B_{ot}\cos\theta_t \qquad (2\text{-}7)$$

Again, $B = \frac{nE}{C_0}$. Therefore, Equation (2-7) can be re-written as

$$-\frac{n_i E_{oi}}{C_0}\cos\theta_i + \frac{n_i E_{or}}{C_0}\cos\theta_r = -\frac{n_t E_{ot}}{C_0}\cos\theta_t$$

Therefore, the reflection coefficient becomes [40],

$$r_{\perp} = \frac{E_{or}}{E_{oi}} = \frac{(n_i\cos\theta_i - n_t\cos\theta_t)}{(n_i\cos\theta_i + n_t\cos\theta_t)} \qquad (2\text{-}8)$$

And, the transmission coefficient can be derived as [40],

$$t_{\perp} = \frac{E_{ot}}{E_{oi}} = \frac{2\,n_i\cos\theta_i}{(n_i\cos\theta_i + n_t\cos\theta_t)} \qquad (2\text{-}9)$$

Similarly, for the parallel polarization it can be shown that [40]

$$r_{||} = \frac{E_{or}}{E_{oi}} = \frac{(n_t\cos\theta_i - n_i\cos\theta_t)}{(n_t\cos\theta_i + n_i\cos\theta_t)} \qquad (2\text{-}10)$$

$$t_{||} = \frac{E_{ot}}{E_{oi}} = \frac{2\,n_i\cos\theta_i}{(n_i\cos\theta_t + n_t\cos\theta_i)} \qquad (2\text{-}11)$$

Again, irradiance is the power of incident electromagnetic wave per unit area. It is also proportional to the field [40]. If R and T are the power reflectance and transmittance of the electromagnetic wave respectively, then for the normal incidence ($\theta_i = 0$) it can be written that:

$$R = r^2 = \left(\frac{n_t - n_i}{n_i + n_t}\right)^2 \qquad (2\text{-}12)$$

$$T = \frac{4n_t n_i}{(n_i + n_t)^2} \qquad (2\text{-}13)$$

Reflectance (R) and transmittance (T) are also called reflectivity and transmissivity respectively. Equation (2-12) is used to theoretically simulate the proposed sensor spectrum in section 2.5.

2.4 The proposed sensor structure

The complete structure of the proposed sensor is shown in Figure 2.4.1.

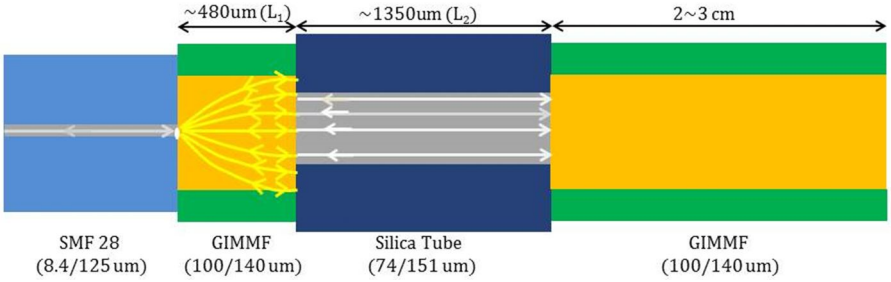

Figure 2.4.1: Structure of the proposed temperature compensated pressure sensor.

Light from an optical source comes into the SMF 28 fiber. A part of this beam is reflected by the air bubble at the splicing junction between the SMF 28 fiber and GIMM fiber. The remaining optical beam enters into the GIMM fiber. As the light propagates down the quarter pitch length of the GIMM fiber, it is collimated due to the graded index profile of the GIMM fiber. At the end of the quarter pitch length, theoretically the light is completely collimated. Part of this collimated beam is again reflected by the splicing junction between the GIMM fiber and silica tube. The remaining collimated beam propagates down the silica tube, reaches the end of the silica tube, and finally is reflected by the splicing junction between the silica tube and GIMM fiber.

There are two cavities in this structure, the GIMM (Graded Index Multimode) fiber cavity and the silica tube cavity. The first cavity is the cavity between the air bubble, and the GIMM fiber/silica tube interface with cavity length L_1. This is named as GIMM (Graded Index Multimode) fiber cavity, and will be used as a temperature sensor. The second cavity is the cavity between the GIMM fiber/silica tube interface and the silica tube/GIMM fiber interface with cavity length L_2. The second cavity contains only silica tube, and is called as silica tube cavity. This silica tube cavity will be used as a pressure sensor. Since the silica tube cavity also inherently responds to temperature, it will be compensated for temperature using the temperature data from the GIMM fiber cavity. Finally, the silica tube cavity responds only to pressure. This composite sensor structure is named as the temperature compensated pressure sensor.

In the proposed sensor structure, the GIMM fiber cavity serves two purposes. First of all, it collimates the incoming light by the graded index profile of the quarter pitch length of GIMM fiber. This collimation is very crucial for the optical beam to propagate within the silica tube which has no light guiding capability. Without this collimation mechanism, the divergence of light during the propagation through the silica tube would be so high that eventually almost no light would be reflected back from the end of the silica tube (silica tube/GIMM fiber interface). Secondly, the GIMM fiber cavity acts as a temperature sensor, and is used to compensate the temperature response of the silica tube cavity.

2.5 Theoretical analysis of the sensor signal

It is well known that whenever there is a change of refractive index at any interface, some light will be reflected back, and the remaining will be transmitted through that interface [40]. The amount of light that will be reflected, or transmitted can be calculated by using Equation (2-12) and (2-13) respectively. Figure 2.5.1 illustrates all the reflections in the proposed sensor structure.

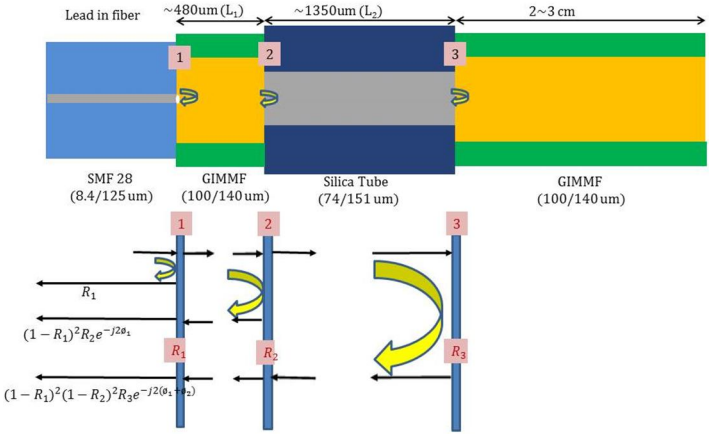

Figure 2.5.1: Schematic of the sensor structure (top), reflections from several interfaces (bottom).

It can be noticed from Figure 2.5.1 that between the reflective interfaces 1 and 2, there is only GIMM fiber. Again, between the reflective interfaces 2 and 3, there is only silica tube. Since each cavity is bounded by two reflective interfaces, this structure contains three (3) reflective interfaces (reflective interfaces 1, 2 and 3) and two cavities (GIMM fiber cavity and silica tube cavity). In the proposed sensor structure, the air bubble is the first reflector at the SMF 28 fiber/GIMM fiber interface (reflective interface 1). The second reflector is at the GIMM fiber/silica tube interface (reflective interface 2). The final reflector is at the silica tube/GIMM fiber interface (reflective interface 3). When, the reflections from the reflective interfaces 1 and 2 are in phase, they will then interfere constructively. Similarly, if the reflections from the reflective interfaces 2 and 3 are in phase, they will also interfere constructively. All the reflected beams combine, form an interference pattern, and can be detected by the integrated detector of Sm125.

Assuming the reflective interfaces 1, 2 and 3 have reflectance R_1, R_2 and R_3 (in this case, $R_2 = R_3$) respectively, and the corresponding cavity lengths are L_1, L_2 and L_3, where $L_3 = L_1 + L_2$. Now for the proposed sensor structure, the R_1, R_2 and R_3 can be written as (using Equation 2-12):

$$R_1 = \left(\frac{n_{SMF} - n_{airbubble}}{n_{SMF} + n_{airbubble}}\right)^2, R_2 = \left(\frac{n_{GIMMF} - n_{Silica\ Tube}}{n_{GIMMF} + n_{Silica\ Tube}}\right)^2, R_3 = R_2$$

where $n_{SMF}, n_{GIMMF}, n_{Silica\ Tube}, n_{airbubble}$ are the refractive indexes of the single mode fiber, graded index multimode fiber, silica tube and air bubble respectively. However, the silica tube has no light guiding capability, containing air inside the tube. Therefore, it can be considered that the silica tube has the refractive index of air: $n_{Silica\ Tube} = n_{airbubble} \cong 1$.

In this theoretical analysis, it will be considered that there are only three reflected rays, and there are no multiple reflections. The first ray is the ray that is reflected by the reflective interface 1, and has normalized energy R_1. The second ray travels a distance L_1 , and is reflected by the reflective interface 2. Therefore, the second ray travels a total distance of $2 * L_1$ and changes the total phase by $2\emptyset_1$. The normalized energy of this ray is [40]: $(1 - R_1)^2 * R_2 e^{-j2\emptyset_1}$

The third ray travels a total distance of $(L_1 + L_2)$, and then is reflected by the reflective interface 3. Therefore, the third ray travels a total distance of $2 * (L_1 + L_2)$, and changes the total phase by $2 * (\emptyset_1 + \emptyset_2)$. The normalized energy of this ray is [40]: $(1 - R_1)^2 * (1 - R_2)^2 * R_3 e^{-j2(\emptyset_1 + \emptyset_2)}$

Now, the sum of the normalized energy of these three rays will give the total optical beam energy received by the detector. This total energy can be written as [40],

$$E = R_1 + (1 - R_1)^2 * R_2 e^{-j2\emptyset_1} + (1 - R_1)^2 * (1 - R_2)^2 * R_3 e^{-j2(\emptyset_1 + \emptyset_2)} \qquad (2\text{-}14)$$

Again, the normalized intensity is [40],

$$I = E \times E^* \qquad (2\text{-}15)$$

where $E^* = R_1 + (1 - R_1)^2 * R_2 e^{+j2\emptyset_1} + (1 - R_1)^2 * (1 - R_2)^2 * R_3 e^{+j2(\emptyset_1 + \emptyset_2)}$ (2-16)

Equation (2-15) can now be re-written as,

$$I = \{(R_1 + (1 - R_1)^2 * R_2 e^{-j2\emptyset_1} + (1 - R_1)^2 * (1 - R_2)^2 * R_3 e^{-j2(\emptyset_1 + \emptyset_2)})\} \times$$

$$\{(R_1 + (1 - R_1)^2 * R_2 e^{+j2\emptyset_1} + +(1 - R_1)^2 * (1 - R_2)^2 * R_3 e^{+j2(\emptyset_1 + \emptyset_2)})\} \qquad (2\text{-}17)$$

The intensity (I) in Equation (2-17) contains all the possible reflections in the proposed sensor structure. Therefore, this equation can be used to theoretically simulate the proposed sensor spectrum. Later, the simulated spectrum is used to calculate the FFT (Fast Fourier Transform). The FFT of the real sensor spectrum and the simulated sensor spectrum is included in section 3.5 of Chapter 3.

2.6 Optical Path Difference (*OPD*) demodulation

Precise *OPD* (optical path difference) demodulation is the most crucial to accurately measure pressure or temperature. If n and L are the refractive index and cavity length respectively, then the OPD of a cavity can be written as [41],

$$OPD = 2 * n * L \qquad (2\text{-}18)$$

After normalization and removal of the DC component, the sensor spectrum usually has the following sinusoidal form [42-44],

$$I \sim \cos(k * OPD + \emptyset) \qquad (2\text{-}19)$$

where φ is the additional phase and k is the wave number. The phase term is due to the mode coupling effect, and usually not constant. However, if a sensor is perfectly fabricated (cleaved fiber end-face is exactly vertical, fibers are precisely aligned and perfectly spliced, etc.), the phase term variation would be significantly small [20].

The peak tracing and *OPD* demodulation software developed at CPT (Center for Photonic Technology), Virginia Tech is used in this research. At first, the *OPD* is crudely estimated by locating the peak. Then, the phase can be predicted using Equation (2-19). In the next step, first order approximations are used to minimize the gap between the estimated results and real data [20]. If n and K_n are the fringe order and peak positions respectively, then the interference peaks satisfy the following equation.

$$K_n * OPD + \emptyset = 2\Pi n \qquad (2\text{-}20)$$

Now, the first order OPD^1 can be calculated by using the K_n (n) relationship. The OPD^1 and pre-calibrated phase [42] are now used to calculate the peak positions of the interference spectrum.

$$K_n{}' * OPD^1 + \emptyset = 2\Pi n \qquad (2\text{-}21)$$

If the *OPD* estimation error is low ($\Delta OPD < \lambda/2$) and the total phase is small ($\leq \mp\pi$), second order estimated OPD^2 can provide even more accurate results [20].

$$OPD_2 = \frac{K_n{}'}{K_n} \times OPD_1 \qquad (2\text{-}22)$$

CHAPTER 3: Miniature temperature compensated pressure sensor

3.1 Miniature Fiber-optic temperature compensated pressure sensor

The design and development of a sensor that can measure both temperature and pressure is one of the most fascinating subjects in the fiber-optic sensor technology. Any contribution in this field would widen up potentially significant research and development efforts, as well as numerous novel applications in the industry [27]. In this chapter, the design, development, and fabrication of a novel miniature fiber-optic sensor is demonstrated through several micro-machining processes. All the components of the sensor system are based on the same type of material, silica. Besides, both the pressure sensor and temperature sensor are multiplexed in the same fiber, making it as an ultra-miniature fiber-optic sensor. The temperature measurement, temperature compensation mechanism, and the pressure measurement are successfully demonstrated through repeatable and multiple sensor tests in the laboratory. The details of the tests are included in Chapter 4.

3.2 Fiber-optic pressure and temperature sensors

The typical fiber-optic pressure sensor consists of a lead-in fiber, the Fabry-Perot cavity, and a diaphragm at the end of the sensor structure [45-48]. Usually, the diaphragm is secured with the sensor assembly through adhesive. The diaphragm responds to the ambient pressure variation, and changes the cavity length (L_1) accordingly. On the other hand, in a typical fiber-optic temperature sensor a section of MMF (Multimode Mode Fiber) is spliced between the two SMFs (Single Mode Fibers). If the ambient temperature changes, the cavity length (L_2) changes, and the interferometry signal modulates subsequently. Finally, the modulated signal can be detected by the detector. A typical fiber-optic pressure sensor and a temperature sensor are shown in Figure 3.2.1(left) and Figure 3.2.1(right) respectively.

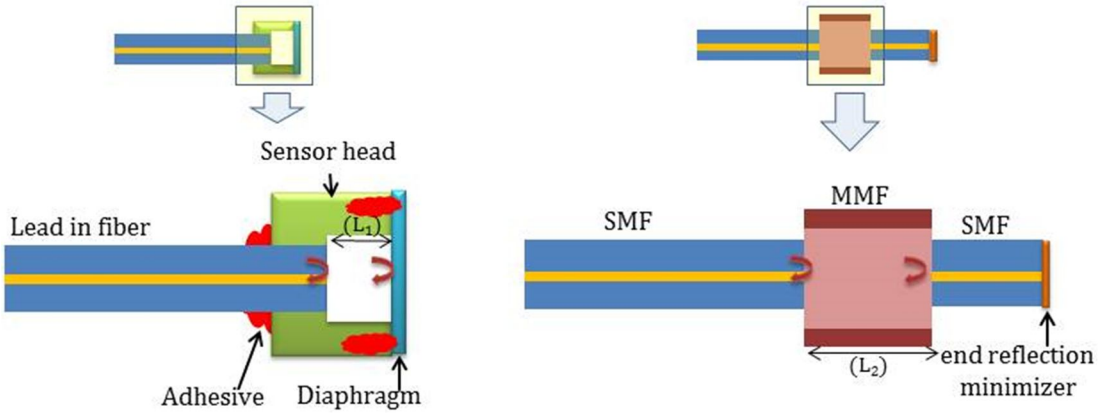

Figure 3.2.1: Typical structure of a fiber-optic pressure sensor (left) [27], temperature sensor (right) *[20]*. Used under fair use, 2014

The conventional pressure sensors have several potential downsides, such as lack of repeatability, potential structure failure, etc. [27]. Some of the major concerns are discussed here: [27]

i) Pressure and temperature response of the adhesive

Since the adhesive attaches the diaphragm with the sensor structure, it is a part of the sensor system. Therefore, the properties of adhesive set a limit on the maximum operating temperature of the sensor. Moreover, the fiber and adhesive are generally composed of different materials. Hence, any

inelastic response of the adhesive material due to the temperature, or pressure variation would unquestionably impair the repeatability, as well as the performance of the sensor [27].

ii) Thermal expansion mismatch

If several types of materials are used within the sensor structure, the reliable and repeatable operation of the sensor becomes further challenging. Dissimilar materials have different softening or melting points, and they can creep at different temperatures. Therefore, they would result thermal expansion mismatch, and development of stress even at the same temperature [27]. Hence, the entire structure might completely fail.

Again, whenever the refractive index change is significant at any interface, the corresponding reflected beam will have higher intensity. Since, the core of SMF and MMF has nearly the same refractive index (low refractive index contrast), the typical fiber-optic temperature sensor (as shown in Figure 3.2.1, right) suffers from a low-reflection level from the SMF/MMF interface.

However, in the proposed sensor structure, all the materials used are fused silica. Hence, the thermal expansion mismatch issue is minimized. Moreover, fusion splicing is used to connect the various segments of the sensor structure. Therefore, the fabricated sensor is free from adhesive too. The proposed sensor is designed to have high refractive index contrast in all the reflection interfaces (for example, SMF/air bubble interface, GIMM fiber/silica tube interface, etc.). This ensures that all the reflected signals will have higher intensity.

3.3 Micromachining techniques

Several fiber micro-machining processes are adopted to fabricate the proposed miniaturized sensor structure. The detailed discussions of the techniques are included here: [27].

i) Precision cleaving

ii) Wet chemical etching

iii) Special fusion splicing (with optimized parameters)

i) Precision cleaving

High-quality cleaving is an essential pre-requisite for the successful splicing. The process begins with a microscopic scratch by a sharp blade, followed by the crack propagation along the fiber. The result is a flat and smooth fiber end surface [27]. Figure 3.3.1 illustrates the micrograph of a well cleaved single mode fiber (corning SMF 28) end-face.

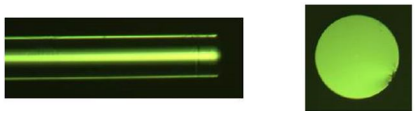

Figure 3.3.1: Micrograph of a cleaved SMF 28 fiber end-face: side view (left), top view (right).

ii) Wet chemical etching

Germanium (Ge) doped silica is etched faster than the pure silica in the HF (hydrofluoric acid) solution [49-51]. The corning SMF 28 fiber is selected for this wet chemical etching. The core of the SMF 28 fiber consists of Germanium doped silica (SiO_2+GeO_2), whereas the cladding is of pure silica

(SiO_2). Whenever the stripped and cleaved fiber-end is etched in the HF solution, the differential etch rate between the core and cladding results in a hollowed pit in the core of the fiber [24]. The cleaved end of a corning SMF 28 fiber before and after the HF etch is observed under the microscope, and is shown in Figure 3.3.2 (left) and Figure 3.3.2 (right) respectively. The HF (Hydrofluoric acid) from ACROS ORGANICS (Hydrofluoric acid for analysis, 48% to 51% solution in water) is used for this etching process.

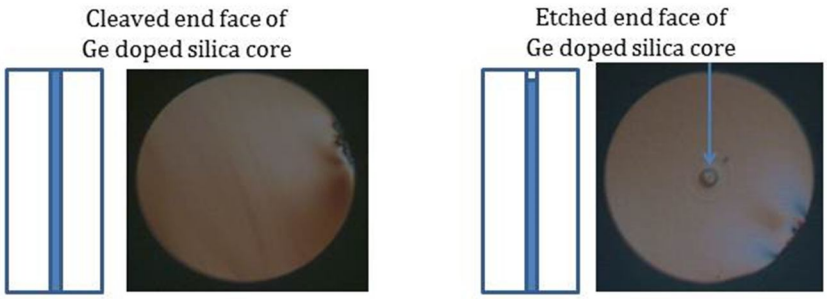

Figure 3.3.2: Cleaved end-face of SMF 28 fiber before etch (left), after etch (right).

The total volume of etch depends on the etch duration, and type or geometry of the fiber. Figure 3.3.3 shows how the etch duration affects the total etch volume for a multimode fiber.

Figure 3.3.3: Multimode fibers etched for: 1 minute (left), 2 minutes (center) and 5 minutes (right).

iii) Special fusion splicing (with optimized parameters)

The latest state of the art fusion splicers are highly sophisticated, and allow superior control during the splicing process. At first, the two fiber ends are stripped, cleaned, and well cleaved. Then, the fibers are precisely aligned by the motorized translational stages located within the splicer. Now, the electric arcs are applied to melt the fiber ends, and the motorized translational stages push the fibers towards each other to complete the splicing. There are many parameters that can be precisely controlled during the splicing process; pre-fuse duration, pre-fuse power, arc power, arc duration, and overlap, etc. are some of the important parameters to mention [27]. Arc power and arc duration regulate how much fiber will melt, and overlap parameters adjust the gap between the fibers [27]. By using the optimized splicing parameters, a flat and uniform splicing junction can be achieved.

During the splicing of special junctions, such as the GIMM fiber/silica tube junction, low arc power and low duration parameters should be used. This is to avoid the potential overheating, and collapse of the silica tube during the splicing process. To fabricate the tiny air bubble at the SMF/GIMM fiber junction, the HF-etched corning SMF 28 fiber along with the low arc power and low duration splicing parameters are used [27]. However, these weak splicing parameters compromise the strength of the spliced-junction, and make the junction susceptible to break during the sensor fabrication, or subsequent handling. Therefore, it is of utmost importance to carefully select the optimized splicing parameters for each of the junctions (SMF/GIMM fiber, GIMM fiber/silica tube junctions, etc.) separately.

Again, if the splicing is perfect, the junction between the similar types of fiber (for example, SMF/SMF, GIMM fiber/GIMM fiber, etc.) is barely distinguishable. On the other hand, if the junctions are of different materials (SMF/GIMM fiber, silica tube/GIMM fiber, etc.), then they are strikingly visible. Figure 3.3.4 (left, center, right) shows the splicing junctions between the SMF/SMF, SMF/GIMM fiber and GIMM fiber/silica tube respectively.

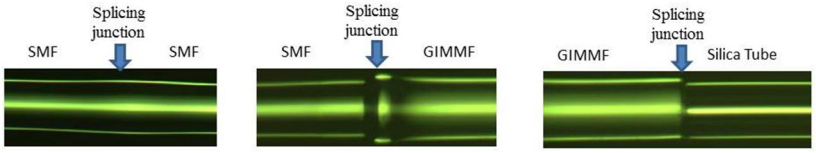

Figure 3.3.4: Splicing junctions: SMF/SMF (left), SMF/GIMMF (center) & GIMMF/Silica tube (right).

3.4 Step-by-step fabrication process

The entire fabrication process can be divided into three steps. At first, the corning SMF 28 fiber is properly cleaved, and then wet chemically etched in HF to form a hollowed pit in the core of the fiber [24]. This step is followed by fusion splicing of the etched SMF 28 fiber with a non-etched GIMM fiber (Ofs optical fiber; MM 100/140/245). As a result, an air bubble is formed at the splicing junction. The other end of the GIMM fiber is then cleaved precisely (Fujikura CT32 high precision cleaver is used) at the quarter pitch length. The quarter pitch length of the GIMM fiber collimates the optical beam, and serves as the GIMM fiber cavity. Now, a cleaved silica tube (Polymicro technologies; 151.1/74.2 OD/ID) is spliced with the quarter pitch GIMM fiber by using optimized fusion splicing parameters. The other end of the tube is cleaved at the desired silica tube cavity length by using an Olympus microscope, and a high precision cleaver equipped with an adjustable linear stage. Finally a MMF (preferably a GIMM fiber with a non- quarter pitch length) is fusion spliced with the silica tube, and this concludes the sensor fabrication process. Detailed discussions of all the fabrication steps are included in the following:

i) Step 1

At the beginning, a stripped and well cleaved corning SMF 28 fiber is etched in the 48%~50% HF solution (Hydrofluoric acid for analysis, 48%~51% solution in water from Acros Organics) for 2 minutes. The differential etch rate between the core and cladding results in a hollowed pit in the core of SMF 28 fiber [24]. Then, the etched SMF 28 fiber is cleaned using DI (deionized) water. Figure 3.4.1 shows the schematic (left) and micrograph (right) of a stripped and well cleaved SMF 28 fiber. The HF-etched SMF 28 fiber and the cleaved GIMM fiber before the fusion splicing are also elucidated in Figure 3.4.2.

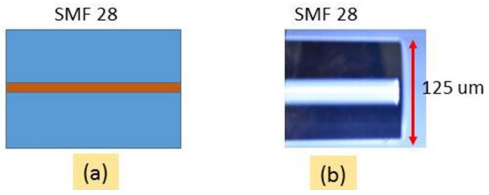

Figure 3.4.1: Cleaved SMF 28 fiber end: (a) schematic, (b) micrograph.

I. (a): The SMF 28 fiber is stripped, and then well-cleaved by using a high precision cleaver.

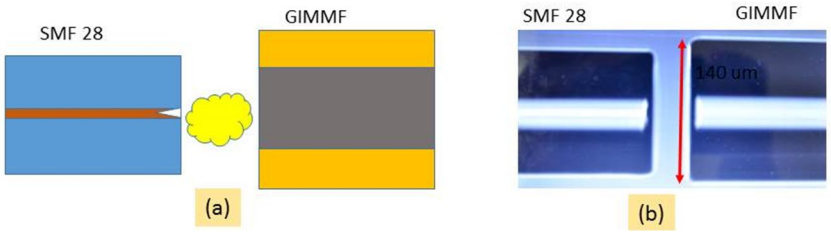

Figure 3.4.2: HF-etched SMF 28 fiber and cleaved GIMMF: (a) schematic, (b) micrograph.

I. (b): *The HF-etched SMF 28 fiber is ready for fusion splicing with a cleaved GIMM fiber.*

ii) Step 2

The next fabrication step is the fusion splicing. The HF-etched SMF 28 fiber is fusion spliced with a cleaved GIMM fiber. As a result, an air bubble is formed at the splicing junction. This air bubble is the first reflection point at the SMF/GIMM fiber junction, and SUMITOMI electric optical fiber fusion splicer is used for the splicing. There should be only one air bubble with submicron order of dimension (diameter on the order of $\leq$1 um) to achieve a superior quality sensor. Weak splicing parameters are the key to fabricate this structure. Now, the GIMM fiber will be cleaved at the quarter pitch length (420 um) [52]. This cleaving operation is conducted under the microscope (Olympus) with a high-precision cleaver equipped with an adjustable linear stage. The microscope is used to position the SMF 28 fiber/GIMM fiber splicing junction on top of the cleaver blade, and the fiber is then precisely adjusted to the desired quarter pitch length through the adjustable linear stage of the cleaver. Finally, the GIMM fiber is cleaved at the quarter pitch length. This quarter pitch GIMM fiber segment works as a temperature sensor, which will be spliced with the silica tube in the next step. Figure 3.4.3 displays that an air bubble is formed at the splicing junction of etched SMF 28 fiber/GIMM fiber.

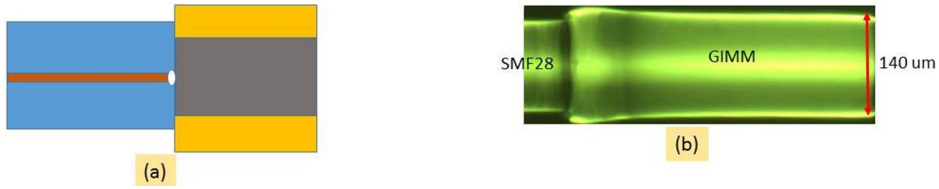

Figure 3.4.3: HF-etched SMF 28 fiber fusion spliced with GIMMF: (a) schematic, (b) micrograph.

II. *The HF-etched SMF 28 fiber is fusion spliced with GIMM fiber, and an air bubble is formed at the splicing junction of SMF 28 fiber/GIMM fiber.*

ii) Step 3

With the completion of step 2, a single mode fiber is spliced with a quarter pitch length of the GIMM fiber. Now, a cleaved silica tube end (OD/ID of 151.1/74.2 from polymicro technologies) will be spliced with the quarter pitch GIMM fiber. As mentioned earlier, separately optimized splicing parameters should be used for the splicing of GIMM fiber and silica tube. This is crucial to avoid any potential deformation of the silica tube during the splicing. Besides, it will also ensure that most of the collimated beam will pass through the silica tube, which is essential for the silica tube to work as a pressure sensor. This GIMM fiber/silica tube junction is the second reflection interface. Now, the silica tube needs to be cleaved at the desired length (typically on the order of ~1500 um for better pressure sensitivity). Again, the cleaving is done under the microscope, and the process is similar to the cleaving procedure described in step 2. Finally, the silica tube end is spliced with a non-quarter pitch GIMM fiber. This silica tube/GIMM fiber junction is the third reflection interface. This concludes the sensor fabrication process.

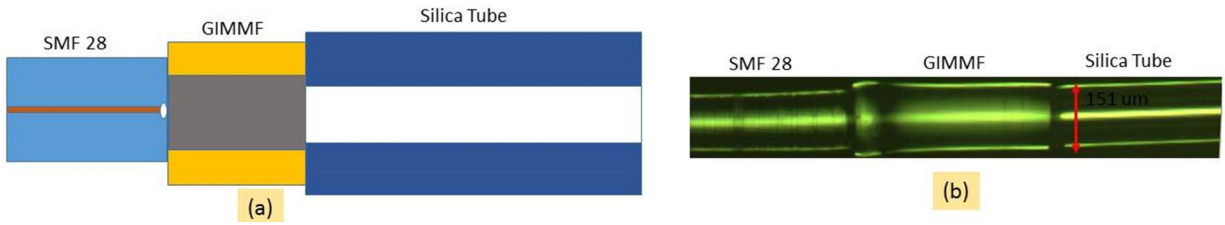

Figure 3.4.4: SMF 28 and 1/4 pitch GIMMF spliced with silica tube: (a) schematic, (b) micrograph.

III. (a): *The SMF 28 fiber and quarter pitch GIMM fiber is spliced with a silica tube by using special fusion splicing parameters.*

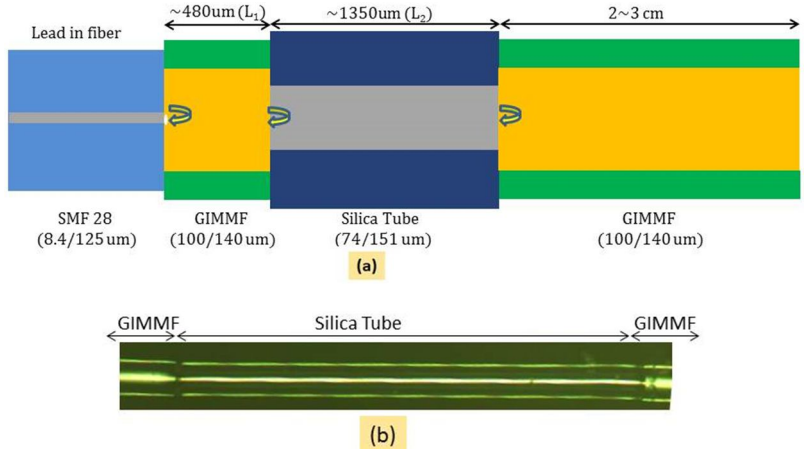

Figure 3.4.5: SMF 28 and 1/4 pitch GIMMF and silica tube spliced with a GIMMF: (a) schematic, (b) micrograph.

III. (b): The SMF 28 fiber and quarter pitch GIMM fiber and silica tube is spliced with a non- quarter pitch length of GIMM fiber, and this completes the sensor fabrication process.

In the complete sensor structure, the collimated optical beam goes through the silica tube, and finally is reflected back from the end of the silica tube (silica tube/GIMM fiber interface). The reflection from the end of the non-quarter pitch GIMM fiber is ignored. Figure 3.4.4 displays the splicing junctions between the SMF 28 fiber/quarter pitch GIMM fiber and quarter pitch GIMM fiber/silica tube. The final step is illustrated by Figure 3.4.5, where the other end of silica tube (SMF 28 fiber-quarter pitch GIMM fiber- silica tube) is spliced with a non-quarter pitch GIMM fiber.

3.5 Spectrum of the fabricated sensor

The complete structure of the fabricated sensor is shown in Figure 3.4.5(a). This structure contains three reflection interfaces. The first reflection is by the air bubble of the SMF 28/GIMM fiber interface; the second reflection is from the GIMM fiber/silica tube interface; and the final reflection is from the silica tube/GIMM fiber interface. If multiple reflections are neglected, there are two cavities: the GIMM fiber cavity (between the air bubble and GIMM fiber/silica tube interface) and the silica tube cavity (between the GIMM fiber/silica tube and silica tube/GIMM fiber interface). All the reflections combine and constitute a composite interference pattern, which is known as sensor spectrum. The spectrum of the fabricated sensor is shown in Figure 3.5.1.

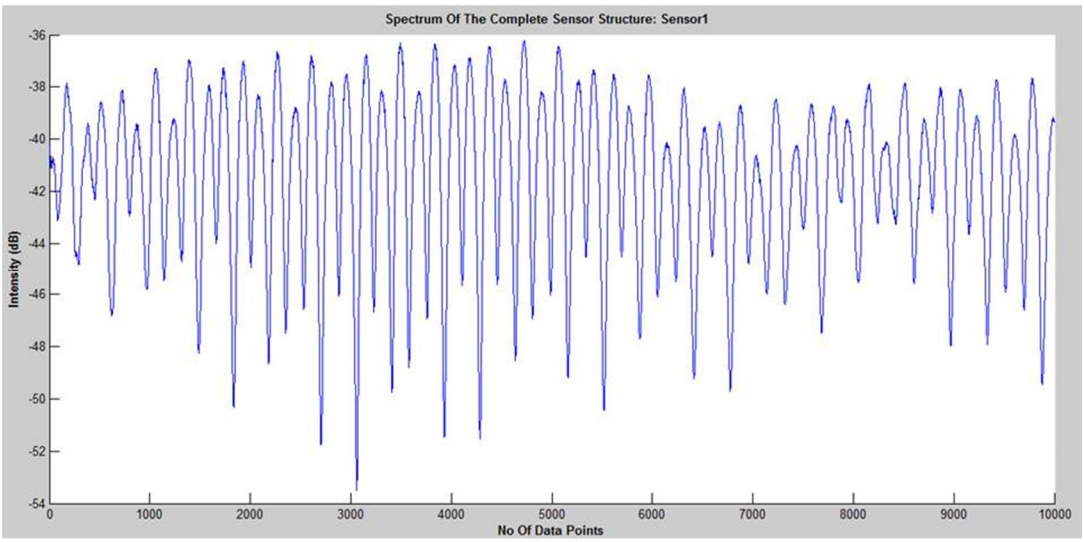

Figure 3.5.1: Spectrum of the fabricated sensor.

Now, if the FFT (Fast Fourier Transform) is conducted on the sensor spectrum, three peaks are expected (one peak corresponds to a single cavity). The first two peaks correspond to the GIMM fiber cavity and the silica tube cavity respectively. The third peak is due to the cavity that is sum of the GIMM fiber cavity and the silica tube cavity. Figure 3.5.2 illustrates the FFT of the fabricated sensor spectrum. Besides, a theoretical simulation of the fabricated sensor structure is also conducted. The corresponding FFT of the simulated sensor spectrum is shown in Figure 3.5.3.

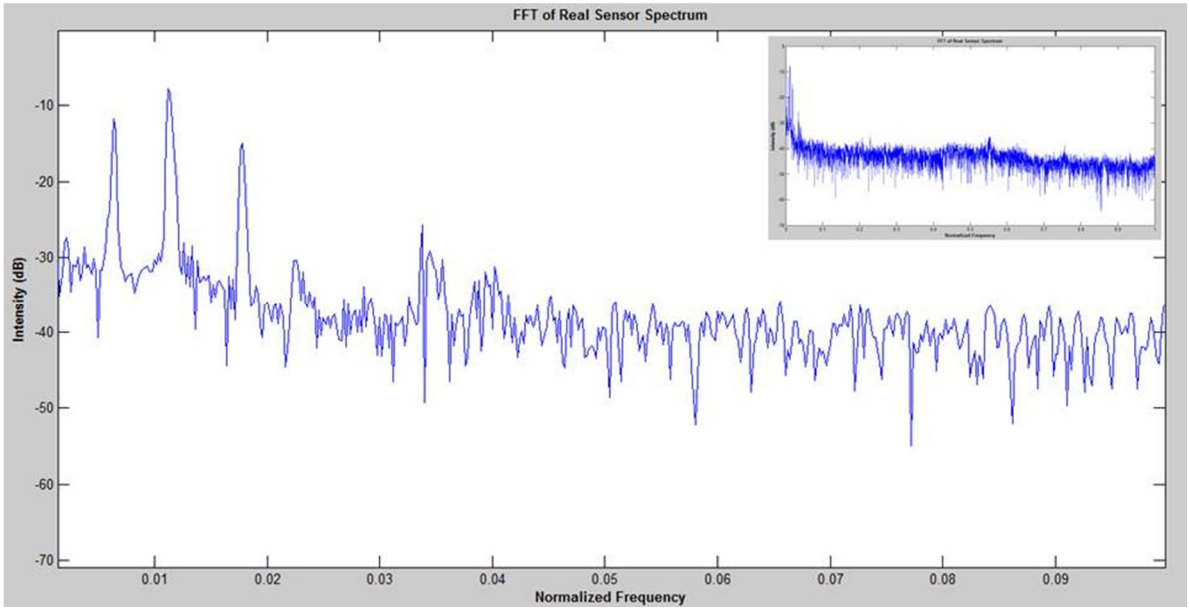

Figure 3.5.2: FFT of the sensor spectrum.

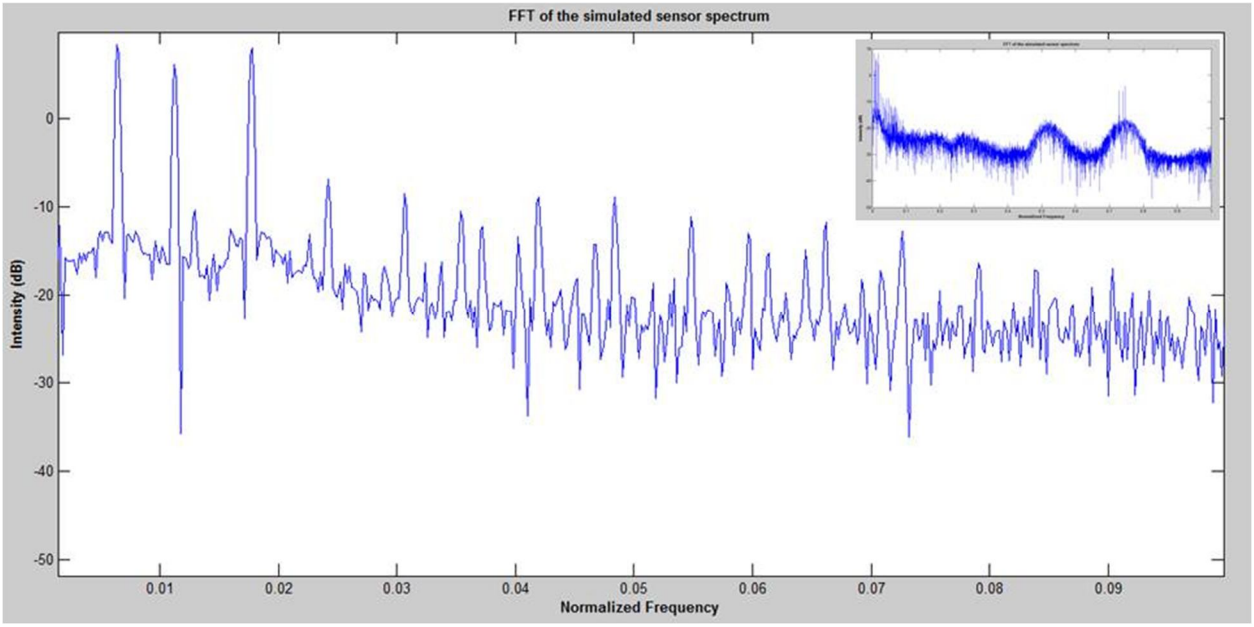

Figure 3.5.3: FFT of the simulated sensor spectrum.

It can be noticed from Figure 3.5.2 that the FFT of the real sensor signal contains some noise. It could be due to the imperfect sensor fabrication process. If a sensor could be perfectly fabricated (exactly vertical cleaving, perfectly smooth splicing, etc.), all the noise would have been eliminated. However, the intensity of the noise is very small compared to the signal intensity. As long as the FFT peaks have a better signal to noise ratio (typical requirement is SNR >6~7 dB), the sensor performance is quite satisfactory.

3.6 Room-temperature stability tests

Once the sensor fabrication is complete, it can be tested for the stability. It is discussed earlier that the fabricated sensor has two cavities: the GIMM fiber cavity and the silica tube cavity. The aim of the stability test is to investigate the fluctuation of *OPD* (optical path difference); the *OPD* of GIMM fiber cavity and silica tube cavity. In this stability test, the sensor spectrum is recorded for the duration of 200 seconds at room temperature and 1 atmospheric pressure. The *OPD* variation of the GIMM fiber cavity for the recorded duration is shown in Figure 3.6.1. The OPD variation of the silica tube cavity is also recorded for 200 seconds duration for the same environmental conditions (at room temperature and 1 atmospheric pressure), as illustrated in Figure 3.6.2.

It can be noticed from Figure 3.6.1 and Figure 3.6.2 that the OPD variations of both the GIMM fiber cavity and silica tube cavity are very small. The standard deviation of OPD is found to be 1.2 nm and 0.2 nm for the GIMM fiber cavity and silica tube cavity respectively. A significant amount of this *OPD* variation could be due to the small temperature variation during the data-recording period. Therefore, both the temperature sensor (GIMM fiber cavity) and the pressure sensor (silica tube cavity) can be considered as essentially stable.

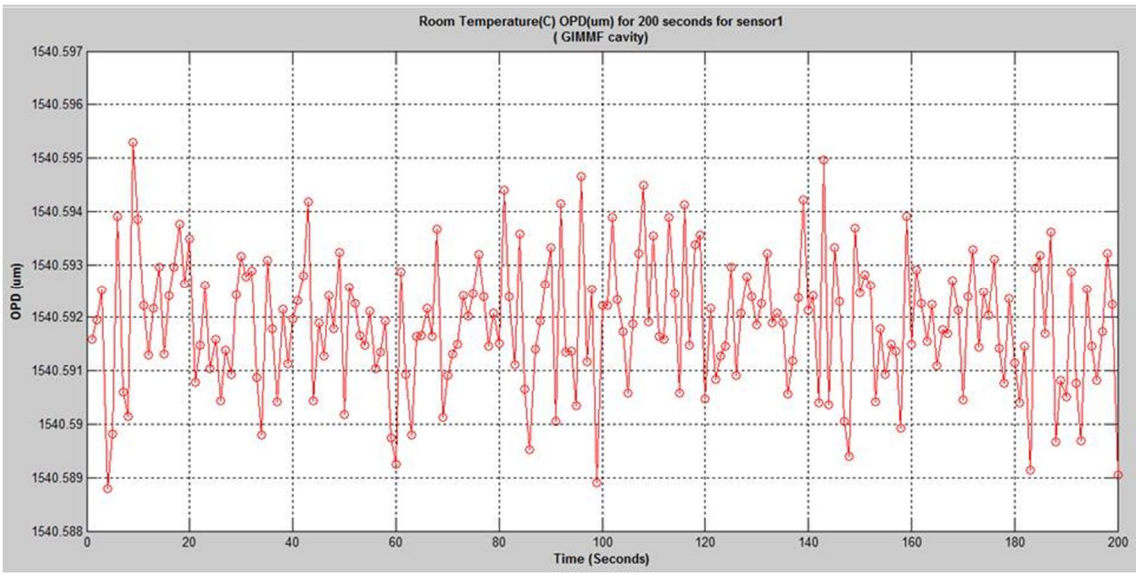

Figure 3.6.1: Room-temperature OPD variation of GIMMF cavity for 200 seconds duration (Sensor 1).

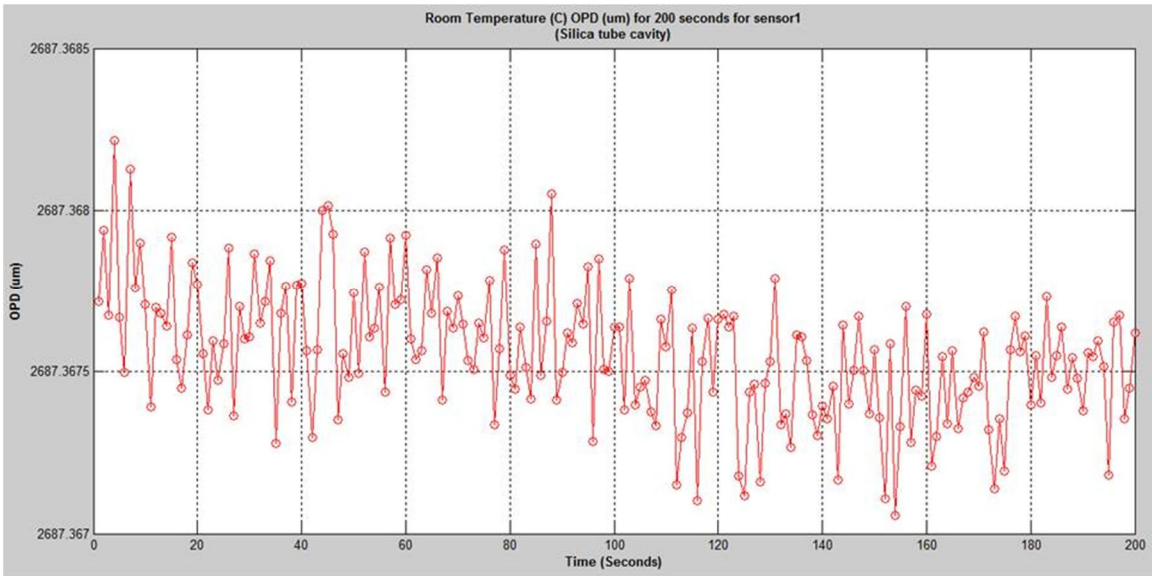

Figure 3.6.2: Room-temperature OPD variation of silica tube cavity for 200 seconds duration (Sensor 1).

CHAPTER 4: Laboratory tests of the fabricated sensor

The fabricated sensor is tested in the laboratory to demonstrate its capability to measure temperature and pressure. The sensor along with a co-located thermocouple is placed within a pressure chamber. The pressure chamber is then placed within a box furnace. The furnace has a built-in thermocouple and a display to show the temperature. This arrangement allows several tests, such as room-temperature pressure test, atmospheric pressure temperature test, and simultaneous pressure and temperature test. For all the tests, fifty consecutive data (one data per second) are recorded at each point of temperature or pressure. Then, the average of each data set (average of fifty consecutive data) is considered as a single point of temperature, or pressure. Multiple tests are also conducted to demonstrate each test's repeatability. By using the software developed at CPT, Virginia Tech, the change of *OPD* (optical path difference) of both the GIMM fiber cavity and the silica tube cavity can be calculated simultaneously from the recorded sensor spectrum. After calibration and parameter modeling, the corresponding temperature and pressure can be accurately measured.

4.1 Experimental setup

Figure 4.1.1 shows the experimental setup for all the pressure and temperature tests of the proposed sensor.

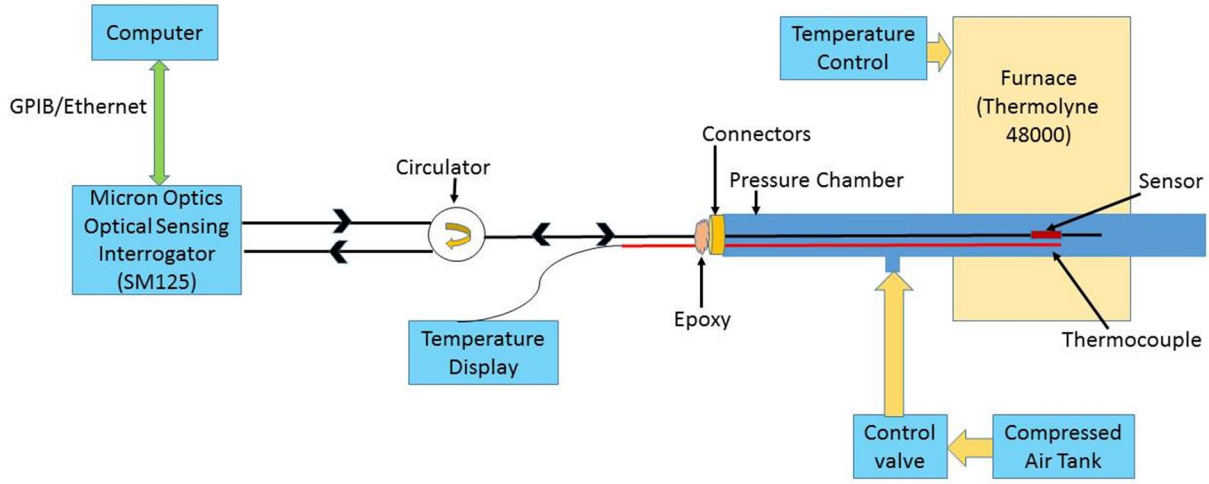

Figure 4.1.1: Experimental setup for the laboratory tests.

Micron optics Optical Sensing Interrogator Sm125 (with sweeping frequency 5Hz and wavelength 1520 nm ~ 1570 nm), which is a Laser source as well as a detector, is used to interrogate the sensor through a circulator. The sensor along with a co-located thermocouple (K-type thermocouple from OMEGA) is positioned within the pressure chamber. The temperature data from this thermocouple will be used for the temperature calibration later. One end of the pressure chamber is connected to a pressure tank (compressed air tank) through a pressure gauge. The other end is sealed using the connectors and adhesive (Miller-Stephenson Epoxy 907 adhesive system). Once the adhesive is cured, the pressure chamber is placed horizontally within the box furnace (Thermolyne 47900 furnace) through the parallel holes. It is crucial to ensure that the segment of pressure chamber which contains the sensor and thermocouple is properly placed in the center region of the box furnace. Since the cylindrical pressure chamber is comparatively longer than the furnace, both ends of the chamber are outside the furnace and can be approximated at the room- temperature. Since the adhesive will be at room temperature, it is not

likely to crack during the temperature tests. The applied temperature and pressure to the sensor are precisely regulated through the digital temperature controller, and the pressure gauge, respectively.

4.2 Temperature response of the graded index multimode fiber (GIMMF) cavity

The optical path difference (*OPD*) between the two reflective interfaces of a Fabry-Perot interferometer can be written by Equation (4-1) [41],

$$OPD_{L1} = 2 * n_e * L_1 \qquad (4\text{-}1)$$

where L_1 is the distance between the two reflective interfaces (between the SMF 28 fiber/GIMM fiber interface and GIMM fiber/silica tube interface in Figure 2.4.1 from Chapter 2), and n_e is the effective refractive index of the GIMM fiber at the operating wavelength. The OPD_{L1} of the temperature sensor (GIMM fiber cavity) can be changed either by the change of the refractive index (n_e), or fiber dimension, or both. Equation (4-1) can therefore be re-written as Equation (4-2) [42].

$$dOPD_{L1}{}^{GIMMF} = 2 * \Delta n_e * L_1 + 2 * n_e * \Delta L_1 \qquad (4\text{-}2)$$

Therefore, $$\frac{dOPD_{L1}{}^{GIMMF}}{L_1} = \left(\alpha_T{}^{GIMMF} + \frac{1}{n_e} * \frac{\partial n_e}{\partial T}\right) * \Delta T = (\alpha_T{}^{GIMMF} + \alpha_{TOC}{}^{GIMMF}) * \Delta T \qquad (4\text{-}3)$$

where $\alpha_T{}^{GIMMF}$ is the coefficient of thermal expansion (CTE) of the graded index multimode fiber, and $\alpha_{TOC}{}^{GIMMF}$ is the thermo-optic coefficient (TOC) of the fused silica fiber: $\alpha_T{}^{GIMMF} = 2 * 10^{-6}$ (1/^{o}C), $\alpha_{TOC}{}^{GIMMF} = 6.8 * 10^{-6}$ (1/^{o}C) [53]. Figure 4.3.2 shows the temperature response of the GIMM fiber cavity.

4.3 Repeatability of the temperature tests

The GIMM fiber cavity of Sensor 1 is tested at 26, 47, 69, 92, 117, 143, 168, 194, 220, 247, 275, 301, 327, 354, 409, 452, 513, 563, 616, and 667^{o}C. The process is repeated twice to investigate the repeatability of temperature response, and the test results are shown in Figure 4.3.1.

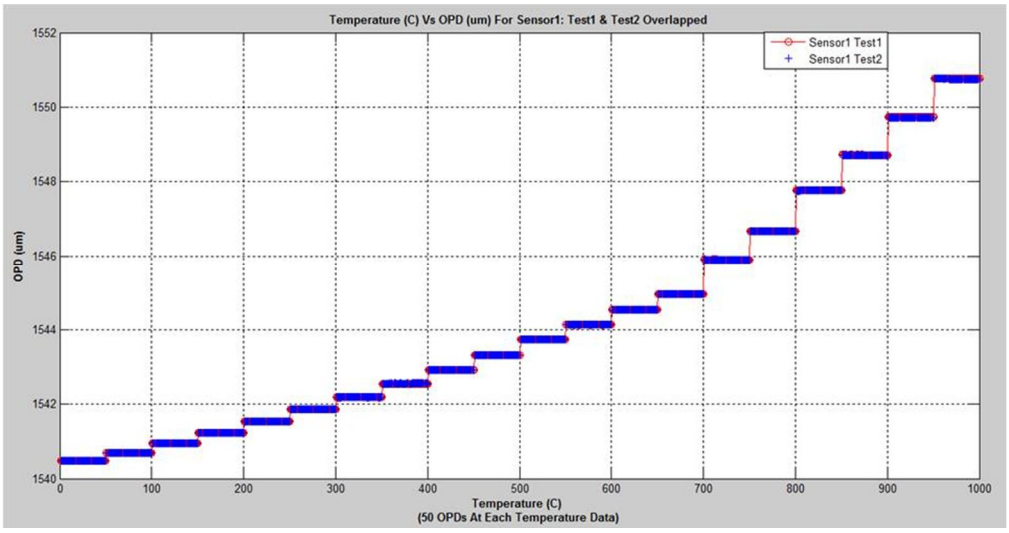

Figure 4.3.1: Temperature response of the GIMMF cavity at 1 atm pressure (Sensor 1).

Each of the tests (test 1 and test 2) in Figure 4.3.1 contains fifty (50) data at each temperature point, and both the test results overlap. Now, the average of fifty (50) data points (average *OPD*) at each temperature is calculated, which corresponds to a specific temperature. The average *OPD* varies depending on the temperature, as shown in Figure 4.3.2. It is also obvious from the figure that both test 1 and test 2 results overlap for the entire temperature range (26~667^{o}C). This is a clear indication of high repeatability of the temperature measurement using the fabricated sensor (GIMM fiber cavity).

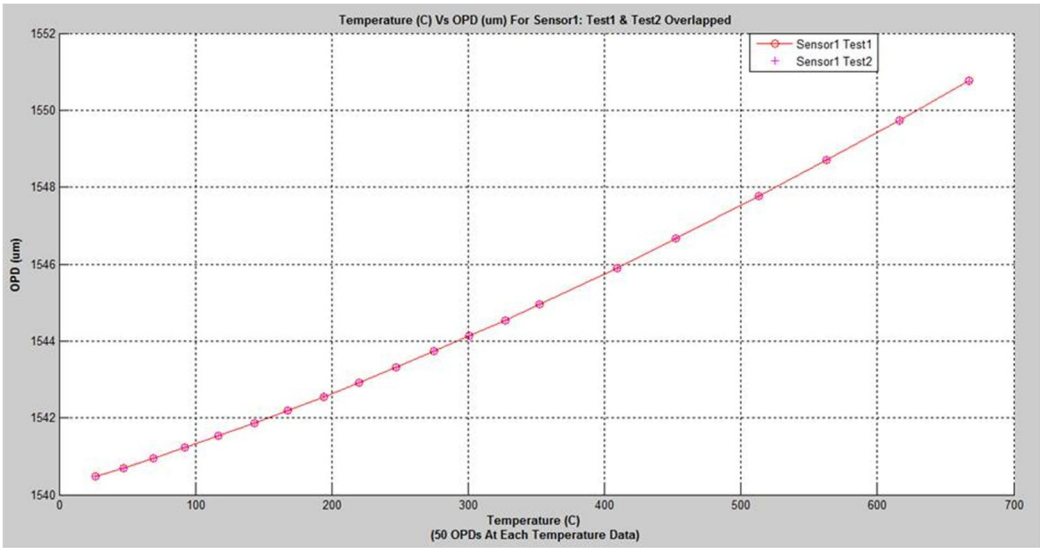

Figure 4.3.2: Temperature response of the GIMMF cavity at 1 atm pressure (Sensor 1).

Now, the temperature response of two separate sensors (Sensor 1 and Sensor 2) will be compared. But, the GIMM fiber cavity length of Sensor 1 and Sensor 2 is not absolutely equal. The minor deviation of cavity length always exists due to the imperfect sensor fabrication process. Therefore, the temperature response of the GIMM fiber cavities should be normalized; the *OPD* of a sensor is divided by the room-temperature *OPD* of the same sensor. Since both the sensors have a similar type of structure and they are made of silica based material, their temperature response should be nearly identical. The normalized *OPD* response due to temperature is illustrated in Figure 4.3.3.

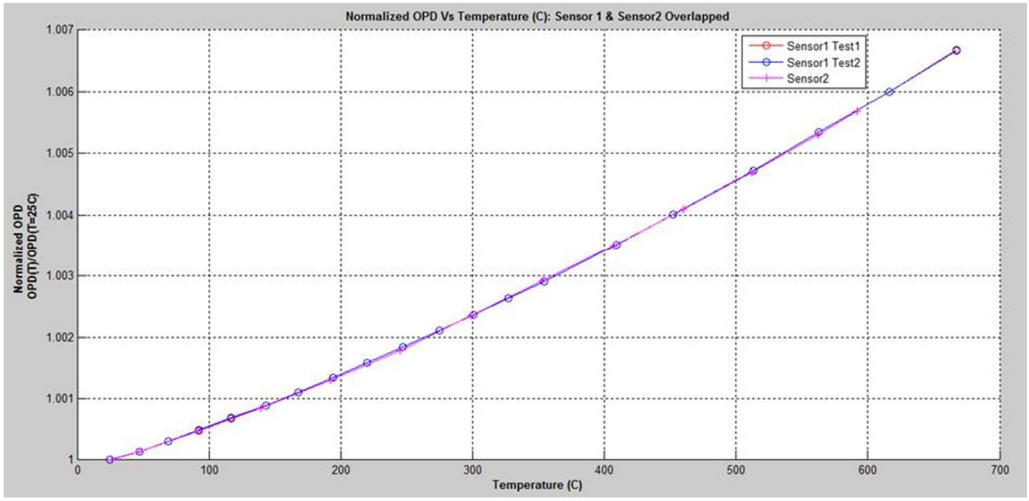

Figure 4.3.3: Temperature dependent normalized *OPD* at 1 atm pressure (Sensor 1 & Sensor 2).

It can be seen from Figure 4.3.3 that the test 1 and test 2 of Sensor 1 and test 1 of Sensor 2, all sensibly overlap. This is an excellent indicator of the repetitive temperature response of the fabricated sensors. Therefore, it can be concluded that the temperature response of the fabricated GIMM fiber cavity (temperature sensor) is very consistent and repeatable.

4.4 Sensitivity and resolution of the temperature sensor

When the temperature changes from 26 to 667^{o}C, the *OPD* of the GIMM fiber cavity changes by 1.028E+04 nm. As the temperature vs. cavity change follows nearly a straight line, the sensitivity can simply be calculated as 1.028E+04 nm/641^{o}C=16.0 nm/^{o}C by using the results of Figure 4.3.2. Again, the standard deviation of the GIMM fiber cavity at room temperature is 1.2 nm (Figure 3.6.1 in section 3.6). Therefore, theoretically the temperature sensor could resolve a temperature change of about 1.2 nm/16.0 nm/^{o}C = 0.08^{o}C within one standard deviation (which contains about 68% of measurements), 0.08*2 = 0.16^{o}C within two standard deviation (95% of measurements fall within two standard deviation), 0.08*3 = 0.24^{o}C within three standard deviation (99.7% of measurements fall within three standard deviation), respectively.

4.5 Temperature calibration of the GIMMF cavity

It is already shown that the GIMM fiber responds well with temperature. Now to use the GIMM fiber cavity as a temperature sensor, the variation of the GIMM fiber *OPD* and the corresponding temperature change needs to be related precisely. This relationship is also known as the temperature calibration of the GIMM fiber cavity. Since the *OPD* of GIMM fiber cavity can be measured immediately, the corresponding temperature can be accurately calculated using the temperature calibration (*OPD* vs. temperature relationship for the GIMM fiber cavity) of the GIMM fiber cavity. Figure 4.5.1 shows the temperature calibration plot for the GIMM fiber cavity.

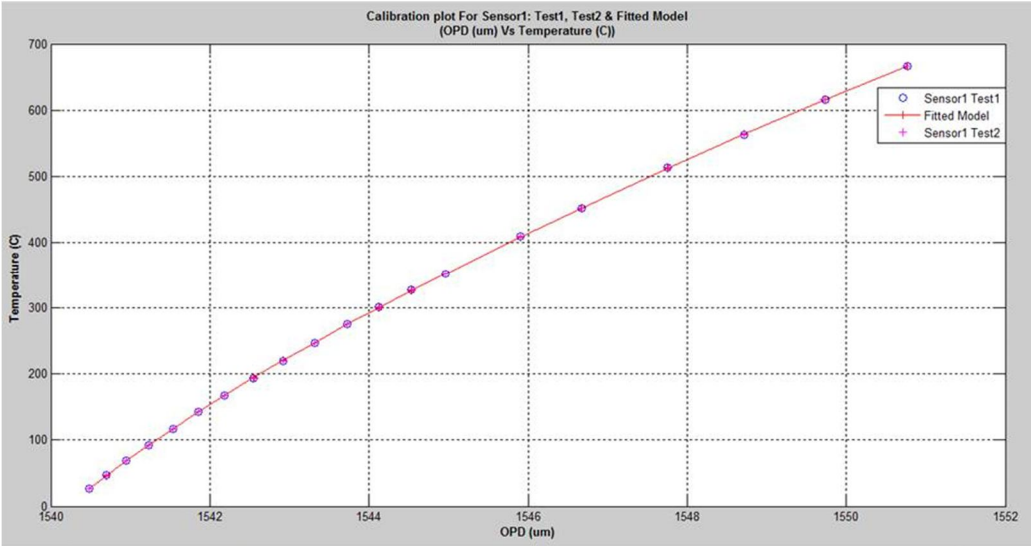

Figure 4.5.1: Temperature calibration (*OPD* vs. Temperature) plot of GIMMF cavity at 1 atm pressure (Sensor 1).

It can be seen from the figure that the calibration model fits well with both the test 1 and test 2 of Sensor 1. Mathematically, the temperature calibration can be expressed by Equation (4-4),

$$T = GF_5 * {OPD_{GIF}}^5 + GF_4 * {OPD_{GIF}}^4 + GF_3 * {OPD_{GIF}}^3 + GF_2 * {OPD_{GIF}}^2 + GF_1 * OPD_{GIF} + GF_0 \quad (4\text{-}4)$$

where OPD_{GIF} is the optical path difference of the GIMM fiber cavity, GF_5, GF_4, GF_3, GF_2, and GF_1 are the temperature coefficients of the GIMM fiber cavity, and GF_0 is a constant. The magnitudes of all the coefficients and constant are included in appendix A.

4.6 Demonstration of temperature measurement by the GIMMF cavity

The temperature calibration will now be used to demonstrate the temperature measurements at several points. The sensor spectrum is recorded at some known temperatures (measured by k-type thermocouple), such as 26, 47, 69, 92, 117, 143, 168, 194, 220, 247, 275, 301, 327, 354, 409, 452, 513, 563, 616, and 667°C, and the test is named as test 1. The process is repeated for four more times, and the tests are named as test 2, test 3, test 4, and test 5 consequently. The *OPD* of the GIMM fiber cavity is now evaluated at each of the temperature points. By using the temperature calibration (Equation 4-4), the corresponding temperature can be calculated. The measured temperature is then compared with the k-type thermocouple reading, and any difference between them is labeled as the deviation of temperature measurement. Figure 4.6.1 demonstrates the temperature measurements, and the corresponding measurement deviations for all the five sets of temperature tests.

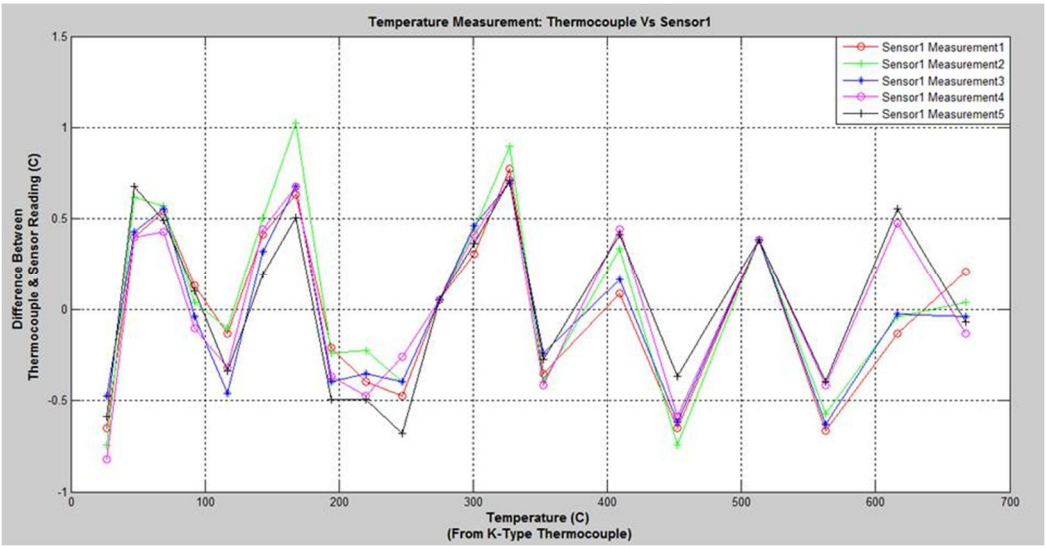

Figure 4.6.1: Demonstration of temperature (°C) measurement by the temperature sensor (Sensor1).

It can be noticed from Figure 4.6.1 that the measurement deviation (the difference between the sensor measurement and k-type thermocouple reading) is within the acceptable limit (approximately within +/- 0.5°C) for all the tests. However, some minor deviation still exists, which could be attributed to several factors. Firstly, the sensor and thermocouple are not exactly at the same location causing some deviation between their measurements. Secondly, since the fitted calibration model is used to measure the temperature, any aberration (from real data) in that model would lead to some deviation in the measurement. Besides, the temperature response of the IFPI sensor is very fast, and more accurate than that of the k-type thermocouple. Therefore, any fast temperature variation may not be reflected in the thermocouple reading, and eventually could contribute to further deviation.

Now, the sensor measurement and the k-type thermocouple reading will be compared. Their relationship is expected to be linear, and it is also obvious from the Figure 4.6.2. The standard deviation

of temperature measurement at several temperature points is also included in the same plot. The y-axis is the reference axis for the standard deviation.

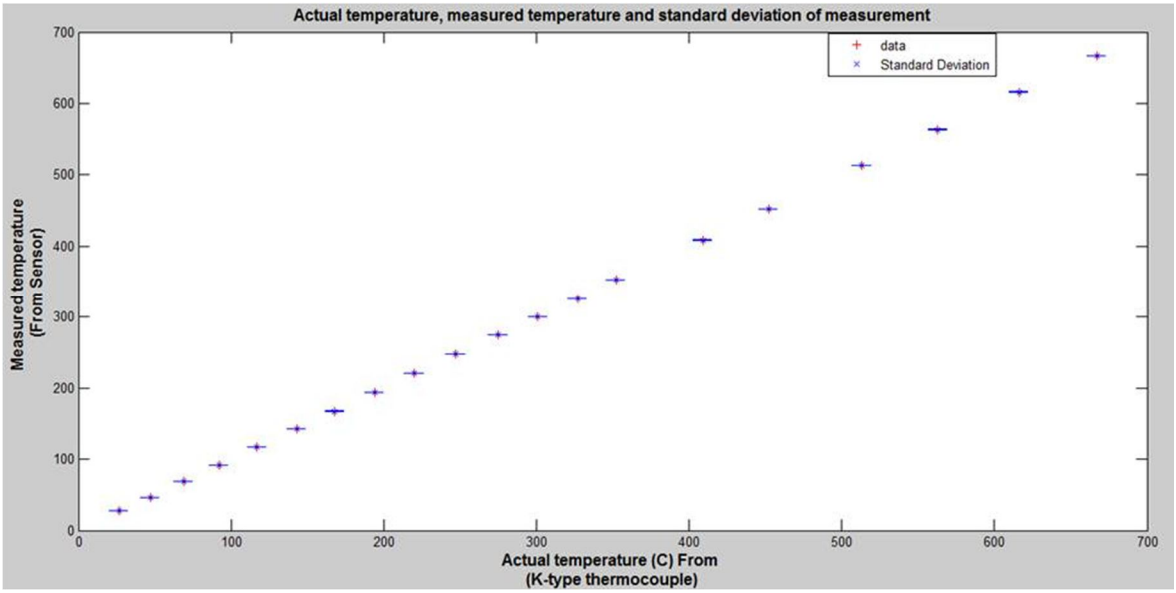

Figure 4.6.2: Temperature measurement (^{o}C): sensor vs. K-type thermocouple & standard deviation of measurement.

Since the standard deviation of all the measurements is very small, a separate plot for the standard deviation will be convenient for further visual inspection. Figure 4.6.3 illustrates the standard deviation of measurement for all the temperature points, which are very small indeed.

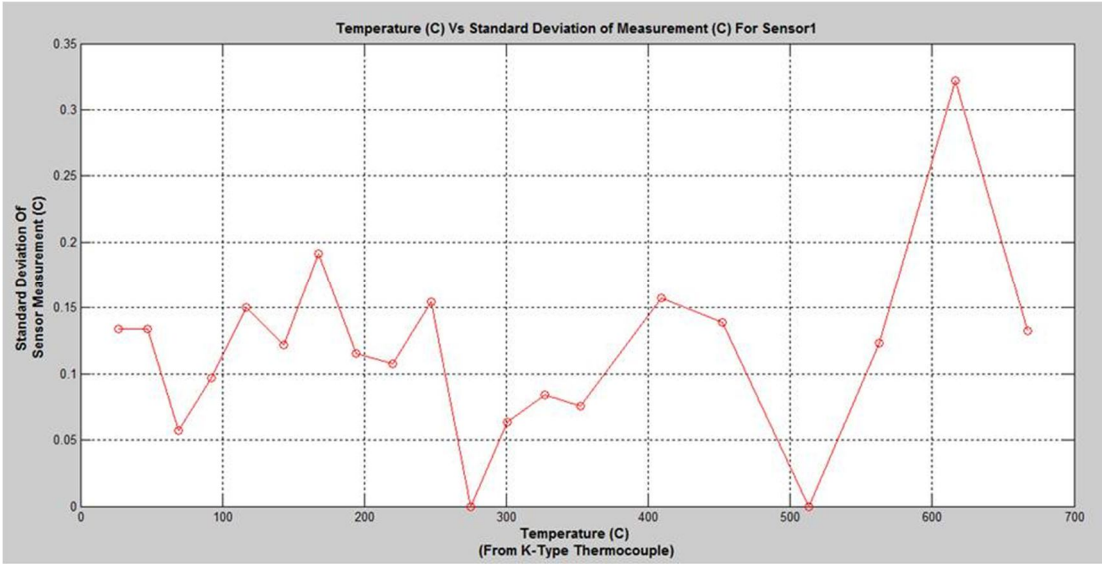

Figure 4.6.3: Standard deviation of temperature measurement for all the temperature points.

In summary, for all the demonstrated temperature measurements, the measurement deviations are very small (approximately within +/- 0.5^{o}C of the thermocouple measurement). The standard deviations are also very small. Therefore, it can be concluded that the temperature sensor is very consistent and acceptably accurate.

4.7 Room-temperature pressure response of GIMMF cavity and silica tube cavity

There are two cavities in this composite sensor structure: the GIMM fiber cavity and the silica tube cavity. The temperature response of the GIMM fiber cavity has already been explained in this chapter. Since the sensor will be tested in a simultaneous pressure and temperature environment, the pressure response of both the cavities should be investigated too. For this test, the pressure chamber is sealed at room temperature. Then, the pressure is varied from 14.7 to 94.7psi through the pressure control valve, and as a result the corresponding cavity length changes. The pressure response of the GIMM fiber cavity at room temperature is depicted by Figure 4.7.1.

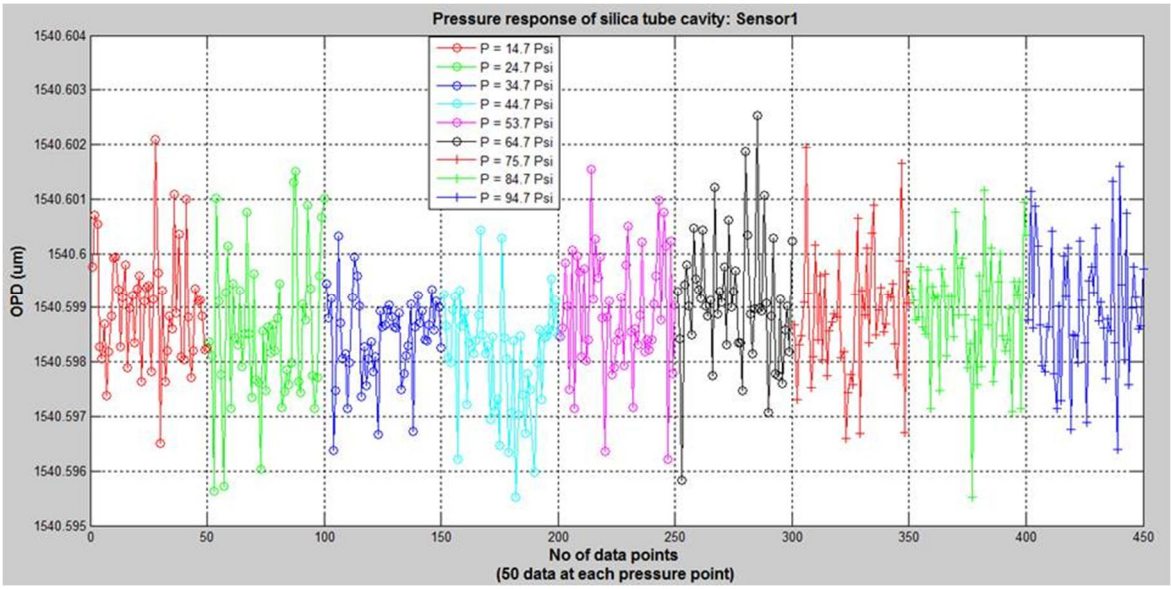

Figure 4.7.1: Pressure (psi) response of the GIMMF cavity at room temperature (Sensor 1).

In Figure 4.7.1, there are fifty (50) successive data for each of the pressure points. It is evident from the figure that although the applied pressure is changed from 14.7 to 94.7psi, the corresponding *OPD* change of the GIMM fiber cavity is insignificant; it is less than 4 nm. Moreover, this *OPD* change is inconsistent, and can be considered as minor random fluctuation. This small random fluctuation could be due to the slight temperature change during the data-recording process. Therefore, it can be approximated with reasonable accuracy that the GIMM fiber cavity is insensitive to pressure, but responsive only to temperature. Therefore, all the temperature measurements by the GIMM fiber cavity are reasonably valid even in a simultaneous pressure and temperature environment.

Now, the room-temperature pressure response of the silica tube cavity is evaluated for the pressure range of 14.7 to 94.7psi, and the corresponding *OPD* changes by 22 nm. This is a significant change of *OPD* compared to that of the GIMM fiber cavity. The pressure response of the silica tube cavity is shown in Figure 4.7.2. It is evident from the figure that the pressure response of the silica tube cavity is quite consistent too. Therefore, the silica tube cavity can be used as a pressure sensor, and the detailed discussions are included later in this chapter.

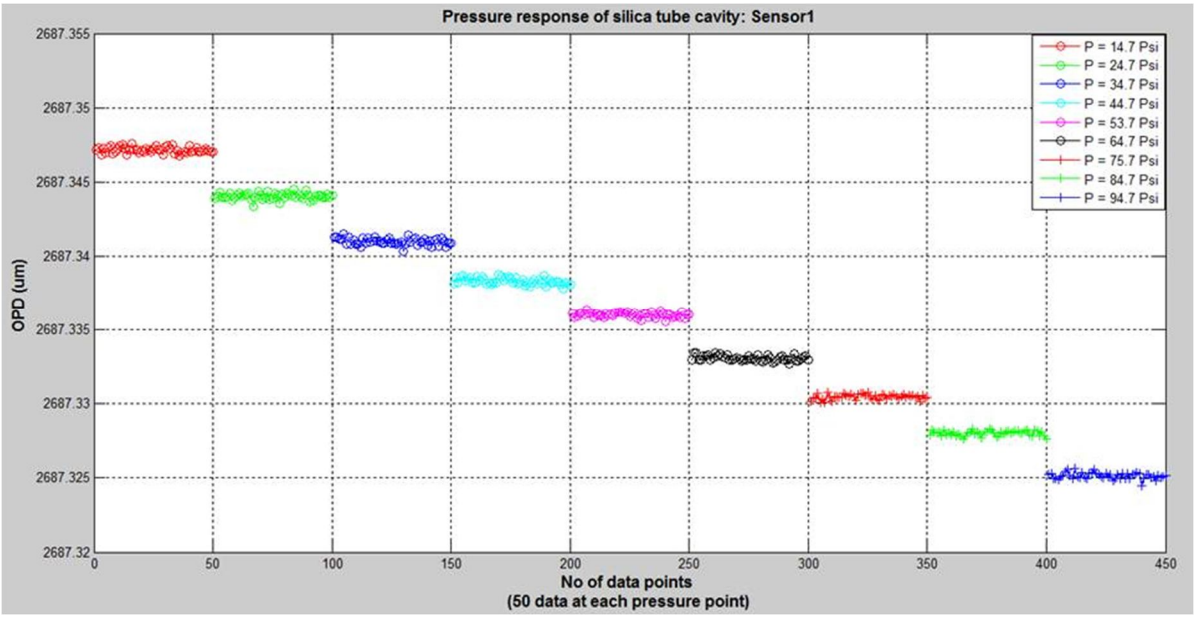

Figure 4.7.2: Pressure (psi) response of the silica tube cavity at room temperature (Sensor 1).

4.8 Temperature response of the silica tube cavity

Two factors can contribute to the change of silica tube cavity length. The first one is the thermal expansion of the silica tube. The second factor is the temperature induced pressure change of the residual gas trapped inside the silica tube cavity. The total change of silica tube cavity length, $\Delta {L_2}^{Silica\ tube}$, can be expressed by Equation (4-5) [27],

$$\Delta {L_2}^{Silica\ tube} = {\alpha_T}^{ST} * {L_2}^{ST} * \Delta T + \Delta L^{ST}(\Delta P_{in}) \qquad (4\text{-}5)$$

where ${\alpha_T}^{ST}$ is the coefficient of thermal expansion (CTE) of the silica tube: ${\alpha_T}^{ST} = 5.4 * 10^{-7}$ (1/^{o}C) [54]. $\Delta L^{ST}(\Delta P_{in})$ is the change of cavity length due to the trapped gas pressure change, and can be written by Equation (4-6) as follows: [55, 56]

$$\Delta L^{ST}(\Delta P_{in}) = \frac{L}{E} * \frac{\Delta P_{in} * {R_2}^2}{{R_2}^2 - {R_1}^2} * (1 - 2 * \upsilon) \qquad (4\text{-}6)$$

where ΔP_{in} is the residual gas pressure change due to the temperature change, $R_1 and\ R_2$ are the inner and outer radiuses of the silica tube respectively, υ is the poison's ratio, L is the silica tube cavity length, and E is the young's modulus of the silica tube material. However, the temperature induced residual gas pressure change can be modeled as follows: [57]

Assuming that for a fixed quantity of ideal gas, the pressure, volume, and temperature are constant. Therefore, it can be written that [58]

$$\frac{PV}{T} = nK = constant$$

Again, assuming that during the constant air-pressure splicing, the temperature changes to 1700^{o}C, then, [57]

$$\frac{P_0 V_0}{T_0} = \frac{P_1 V_1}{T_1}\ , V_1 = 6.62 * V_0$$

Once the splicing is complete, the air is trapped inside the silica tube cavity. If the pressure of the trapped gas is P_1, then

$$P_1 = \frac{P_0}{6.62} = 2.22\ Psi$$

Now, if the temperature rises to T_2, the trapped gas pressure also changes to P_2 [57].

$$P_2 = \frac{P_1}{T_1} * T_2$$

Therefore, the trapped gas pressure inside the silica tube cavity changes by ΔP_{in}, where $\Delta P_{in} = (P_2 - P_1)$ psi. However, the *OPD* change due to the trapped gas pressure change, $[\Delta L^{ST}(\Delta P_{in})]$, is smaller than the temperature induced *OPD* change, $[{\alpha_T}^{ST} * {L_2}^{ST} * \Delta T]$, in Equation (4-5).

4.9 Sensitivity and resolution of the pressure sensor

The pressure sensor responds to both temperature and pressure. At 1 atmospheric pressure, if the temperature changes from 26 to 667^{o}C, the *OPD* of the silica tube cavity changes by 9.922E+02 nm. As the temperature vs. cavity change follows nearly a straight line, the temperature sensitivity of the silica tube can simply be calculated as 9.922E+02 nm/642^{o}C=1.54 nm/^{o}C by using the results of Figure 4.10.1. The standard deviation of the silica tube cavity at room temperature is 0.2 nm (Figure 3.6.2 in section 3.6). Again, the pressure sensitivity of the silica tube cavity dependents on temperature, and is discussed in detail in section 4.10. Therefore, at 23, 301, 406 510 and 612^{o}C, theoretically the pressure sensor can resolve 0.7, 0.8, 1.0, 0.8, and 0.5psi within one standard deviation (68% of measurements fall within two standard deviation), 1.4, 1.6, 2.0, 1.6, 1.0psi within two standard deviation (95% of measurements fall within two standard deviation) respectively.

4.10 Temperature compensation mechanism

It is already shown that the GIMM fiber cavity responds to temperature. However, it is insensitive to pressure. On the other hand, the silica tube cavity responds to both temperature and pressure. The cavity length of the silica tube increases with temperature, but decreases with pressure. Since the purpose is to use the silica tube cavity as a pressure sensor in a simultaneous pressure and temperature environment, the temperature effect needs to be eliminated from the silica tube cavity. By measuring the temperature from the GIMM fiber cavity (which is a temperature sensor) and using that temperature data in the silica tube temperature calibration (Equation 4-7), the silica tube cavity can be compensated for the temperature response. Then, the silica tube cavity response will depend on the temperature dependent coefficients and pressure. Therefore, the corresponding pressure can be calculated. However, the temperature compensation mechanism is essential for the silica tube cavity to use it as a pressure sensor.

Nevertheless, the silica tube cavity does not have the same temperature response as of the GIMM fiber cavity. Hence, the temperature response of the silica tube cavity needs to be modeled properly. Now, by using the recorded sensor spectrum (temperature test at 1 atm pressure and 26 ~ 667^{o}C, 23~612^{o}C), the corresponding silica tube *OPD* is calculated. Figure 4.10.1 shows the differential temperature (temperature w.r.t room-temperature) induced differential *OPD* change (*OPD* w.r.t room-temperature *OPD*) for the silica tube cavity at 1 atm pressure. Three temperature tests are conducted. All the test results and the fitted model sensibly overlap. This fitted model is the temperature calibration of the silica tube cavity, and mathematically can be expressed by Equation (4-7),

$$dOPD(T > 23)_{Silica\ Tube} = ST_{T5} * dT^5 + ST_{T4} * dT^4 + ST_{T3} * dT^3 + ST_{T2} * dT^2 + ST_{T1} * dT + ST_0 \quad (4-7)$$

where $dOPD_{Silica\ Tube}$ is the change of silica tube *OPD* with respect to the room-temperature *OPD*: $dOPD_{Silica\ Tube} = OPD(T) - OPD(T = 23^oC)$. dT is the temperature change with respect to the room-temperature: $dT = T - 23^oC$. ST_{T5}, ST_{T4}, ST_{T3}, ST_{T2}, *and* ST_{T1} are the temperature coefficients of the silica tube cavity, and ST_0 is a constant. The magnitudes of all the coefficients and constant are included in appendix A.

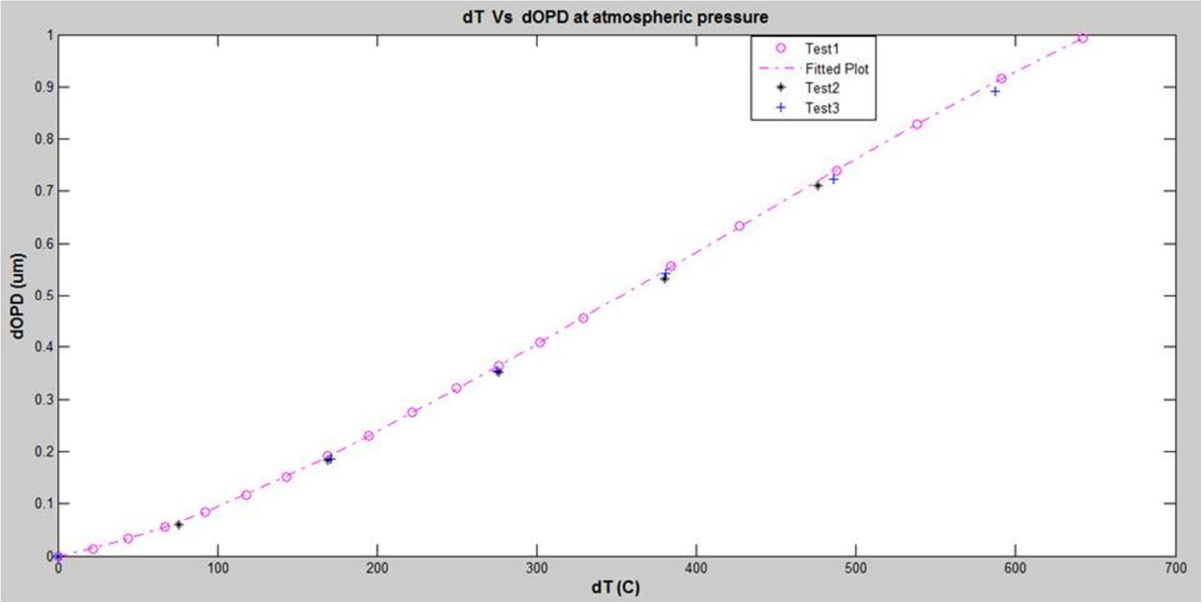

Figure 4.10.1: Temperature response & fitted model for silica tube cavity at 1 atm pressure (Sensor 1).

The sensor will now be tested in a simultaneous pressure and temperature environment. The sensor spectrum is recorded at several known pressure and temperature points. Another set of test is also conducted to probe the repeatability of the measurements. Now, the *OPD* of the silica tube cavity is evaluated at each of the recorded data points. Figure 4.10.2 illustrates a simultaneous pressure and temperature response of the silica tube cavity. In the figure, the same color data points represent the pressure response at a constant temperature. Therefore, different color data points display the pressure response at different temperatures. It can also be noticed that the *OPD* of the silica tube cavity decreases with pressure, but increases with temperature. However, for the applied pressure and temperature range, the temperature response is more dominant compared to the pressure response.

The temperature compensation mechanism of the silica tube cavity will be explained now. The two-step compensation mechanism starts with the temperature measurement by the GIMM fiber cavity (using Equation 4-4). Then, the temperature data is used to calculate the differential *OPD* ($dOPD(T > 23)_{Silica\ Tube}$) of the silica tube cavity (using Equation 4-7). Here, the differential *OPD* is the change of silica tube *OPD* from its room-temperature value (room-temperature *OPD*). The temperature compensation mechanism can be expressed by using Equation (4-8),

$$OPD(P + T)_{ST} = dOPD(T > 23)_{Silica\ Tube} + OPD_{After\ TC} \quad (4-8)$$

where $OPD(P + T)_{ST}$ is the OPD of silica tube cavity due to the simultaneous pressure and temperature, and is a measurable quantity. After temperature compensation, the only unknown term in Equation (4-8) is $OPD_{After\ TC}$.

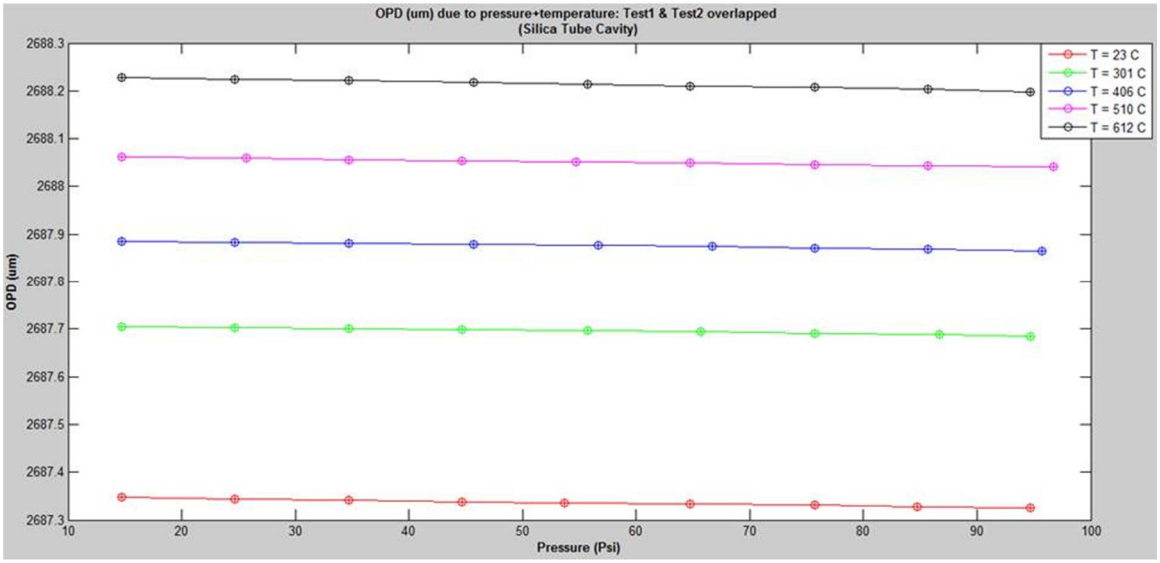

Figure 4.10.2: Silica tube cavity under simultaneous pressure & temperature (Test 1 & Test 2).

The pressure response of the silica tube cavity after temperature compensation is shown in Figure 4.10.3. It can be noticed from the figure that the pressure response of the silica tube cavity is temperature dependent. In other words, different color data points (can be seen as lines) have different slopes. Here, the slope is the change of $OPD_{after\ TC}$ per unit pressure change, $(\frac{dOPD_{after\ TC}}{dP})$, and can be termed as temperature dependent pressure sensitivity; $[S_p(T)]$.

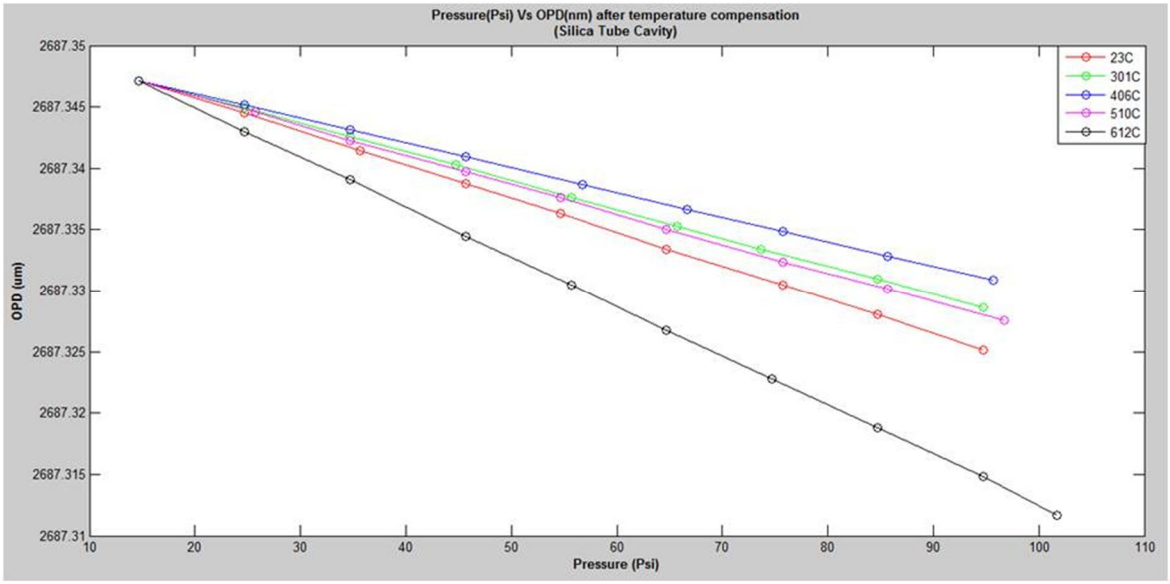

Figure 4.10.3: Pressure response of the silica tube cavity after temperature compensation.

After temperature compensation, the $OPD_{After\ TC}$ of the silica tube cavity is a known quantity, but the pressure is unknown. Therefore, the temperature compensated $OPD_{After\ TC}$ needs to be modeled as a function of pressure. Now, by using the data of Figure 4.10.3 the temperature compensated *OPD* ($OPD_{After\ TC}$) can be mathematically expressed by Equation (4-9),

$$OPD_{After\ TC} = S_P(T) * P_T + C_T\ (T) \quad (4\text{-}9)$$

where C_T (T) is a temperature dependent coefficient, and P_T is the pressure to be measured. Therefore, Equation (4-8) can be written as Equation (4-10).

$$OPD(P+T)_{ST} = dOPD(T > 23)_{Silica\ Tube} + [S_P(T) * P_T + C_T\ (T)\ ] \quad (4\text{-}10)$$

Now, there are two unknowns in Equation (4-9), $S_P(T)$ and P_T. By using the data of Figure 4.10.3, the temperature dependent pressure sensitivity $[S_P(T)]$ is illustrated in Figure 4.10.4.

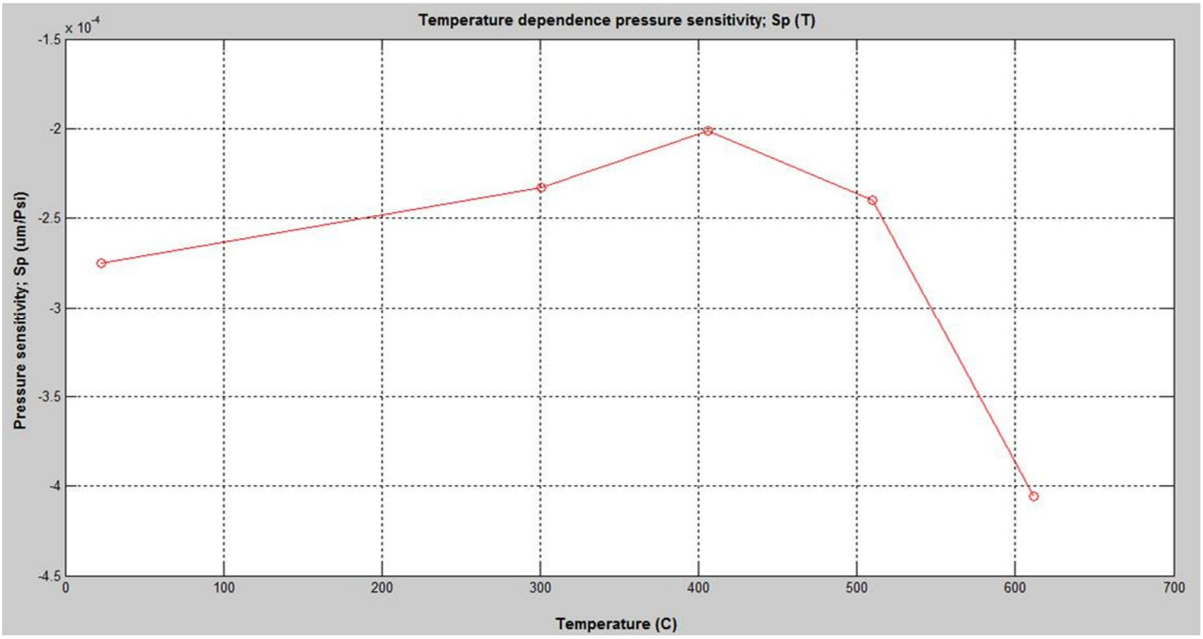

Figure 4.10.4: Temperature dependent pressure sensitivity of pressure sensor (silica tube cavity).

It can be noticed from Figure 4.10.4 that the pressure sensitivity (um/psi) slowly changes with temperature. But there is an abrupt change at 612°C, which could be due to the stress relaxation at such a high temperature (since the sensor was annealed at 520°C). The negative sign in the pressure sensitivity is due to the inverse relationship between the pressure change, and the corresponding silica tube *OPD* change (as the pressure increases, the silica tube *OPD* decreases) at a constant temperature.

Again, at 23°C, Equation (4-9) can be written as Equation (4-11)

$$OPD_{After\ TC}{}^{(T=23c)} = S_P{}^{(T=23c)} * P_T + C_T{}^{(T=23c)}) \quad (4\text{-}11)$$

Similarly, at 301, 406, 510, and 612°C, the $OPD_{After\ TC}$ can be expressed by Equation (4-12), (4-13), (4-14), and (4-15) respectively,

$$OPD_{After\ TC}{}^{(T=301c)} = S_P{}^{(T=301c)} * P_T + C_T{}^{(T=23c)} + dC_{301} \quad (4\text{-}12)$$

$$OPD_{After\ TC}{}^{(T=406c)} = S_P{}^{(T=406c)} * P_T + C_T{}^{(T=23c)} + dC_{406} \quad (4\text{-}13)$$

$$OPD_{After\ TC}{}^{(T=510c)} = S_P{}^{(T=510c)} * P_T + C_T{}^{(T=23c)} + dC_{510} \quad (4\text{-}14)$$

$$OPD_{After\ TC}{}^{(T=612c)} = S_P{}^{(T=612c)} * P_T + C_T{}^{(T=23c)} + dC_{612} \quad (4\text{-}15)$$

where ${C_T}^{(T=23c)}, dC_{301}, dC_{406}, dC_{510,}$ and dC_{612} are the temperature dependent coefficients at 23, 301, 406, 510, and 612°C, respectively. Now, these coefficients (dC_T) will be modeled using the results of Figure 4.10.3. The temperature dependence of dC_T as well as the fitted model is shown in Figure 4.10.5.

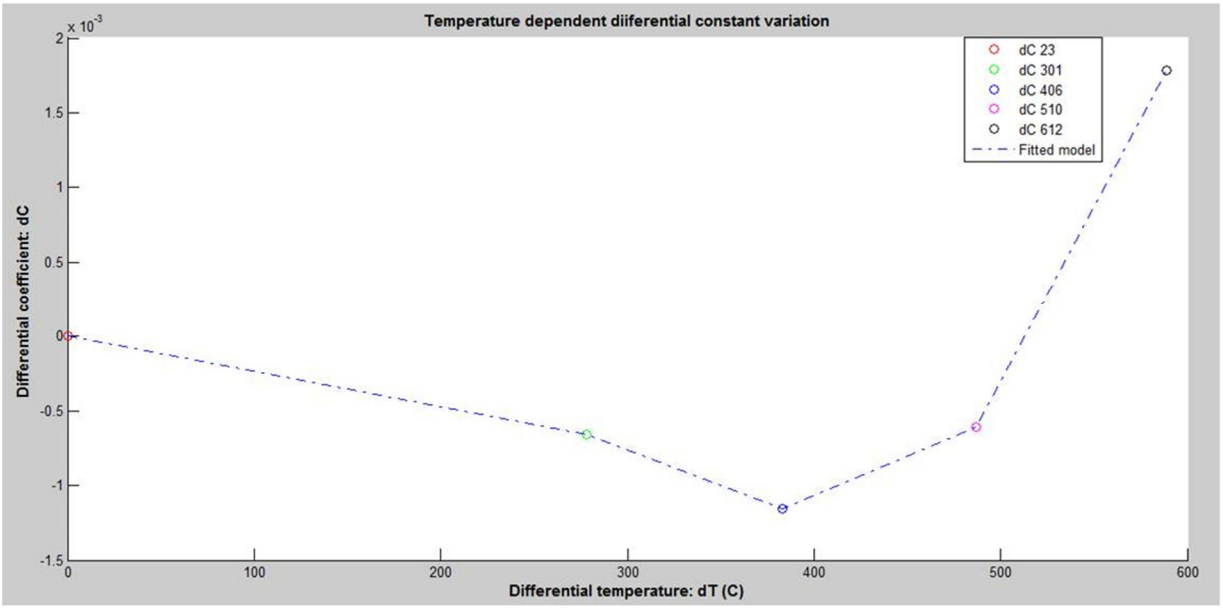

Figure 4.10.5: Temperature dependent coefficients ($dC_T\ s$) for silica tube cavity.

By using the fitted model of Figure 4.10.5, the temperature dependent coefficients can be written by Equation (4-16),

$$dC_T = CT_4 * dT^4 + CT_3 * dT^3 + CT_2 * dT^2 + CT_1 * dT^1 + CT_0 \qquad (4\text{-}16)$$

where dT is the differential temperature (dT = T-23°C), $CT_4, CT_3, CT_2, and\ CT_1$ are the temperature dependent coefficients and CT_0 is a constant. The magnitudes of all the coefficients and constant are included in appendix A.

Therefore, by substituting all the coefficients and constants, Equation (4-10) can be rewritten as the following Equation (4-17).

$$OPD(P+T)_{ST} = [ST_{T5} * dT^5 + ST_{T4} * dT^4 + ST_{T3} * dT^3 + ST_{T2} * dT^2 + ST_{T1} * dT + ST_0] + [S_P(T) * P_T] + [{C_T}^{(T=23c)} + CT_4 * dT^4 + CT_3 * dT^3 + CT_2 * dT^2 + CT_1 * dT^1 + CT_0] \qquad (4\text{-}17)$$

The only term in the left hand side of Equation (4-17) corresponds to the silica tube *OPD* in a simultaneous pressure and temperature environment. In the right hand side, the first terms in the bracket lead to the differential *OPD* due to the temperature change from the room temperature, the second terms in the bracket are the temperature dependent pressure sensitivity and the pressure to be measured, the final terms in the bracket are the temperature dependent coefficients and constant.

4.11 Demonstration of pressure measurement

Now the pressure measurement by the pressure sensor will be demonstrated in a simultaneous pressure and temperature environment. The sensor spectrum is recorded at several known temperature and pressure points. Five tests are conducted, and are named as test 1, test 2, test 3, test 4, and test 5, respectively. The measured pressure is later compared with the recorded pressure.

Therefore, by using Equation (4-11), the measured pressure at a certain temperature (T) can be expressed by Equation (4-18).

$$P_T = \left(\frac{1}{S_P{}^{(T)}}\right) * [OPD_{After\ TC}{}^{(T)} - C_T{}^{(T)} - dC_T] \qquad (4\text{-}18)$$

The pressure measurement at several temperatures is illustrated below:

Pressure measurement at T=23°C

At 23°C, the measured pressure can be written by the following Equation (4-19),

$$P_T = \left(\frac{1}{S_P{}^{(T=23c)}}\right) * [OPD_{After\ TC}{}^{(T=23c)} - C_T{}^{(T=23c)}] \qquad (4\text{-}19)$$

where $S_P{}^{T=23\,C}$ is the room-temperature pressure sensitivity, $C_T{}^{(T=23c)}$ is the room-temperature coefficient, and $OPD_{After\ TC}{}^{(T=23c)}$ is the OPD of the silica tube cavity after temperature compensation. Five separate tests are conducted, and the corresponding pressure measurements are shown in Figure 4.11.1.

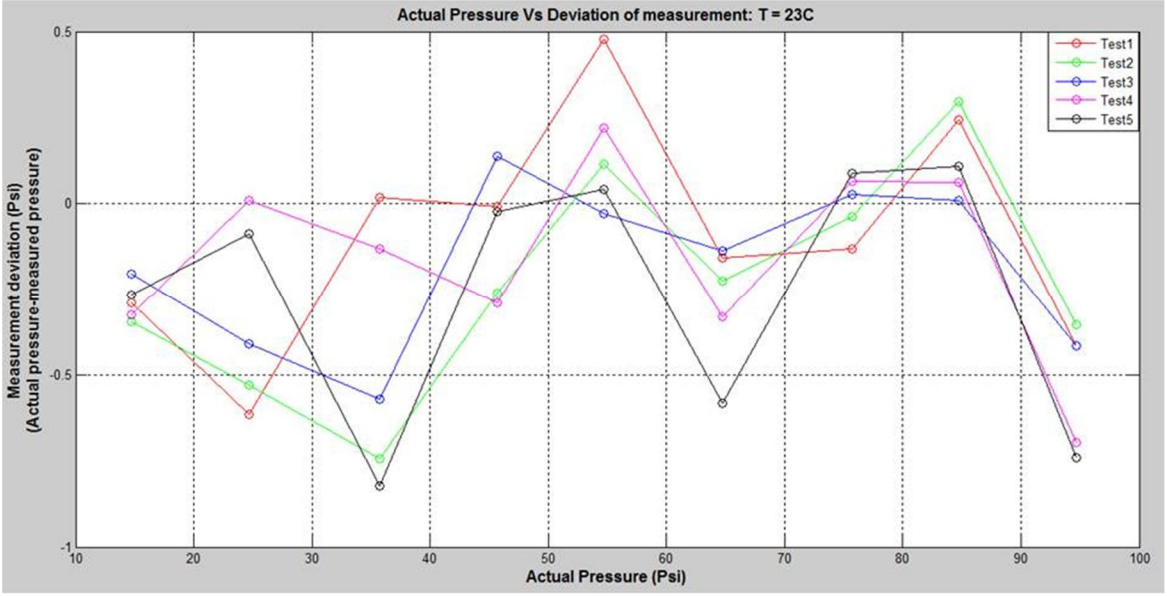

Figure 4.11.1: Actual pressure (psi) vs. measurement error (psi) at 23°C.

The measured pressure and the actual pressure are also compared in Figure 4.11.2. Their relationship is expected to be linear, and is also obvious from the figure. The standard deviation of measurement is also included in the same figure. Here, y axis is the axis for the standard deviation.

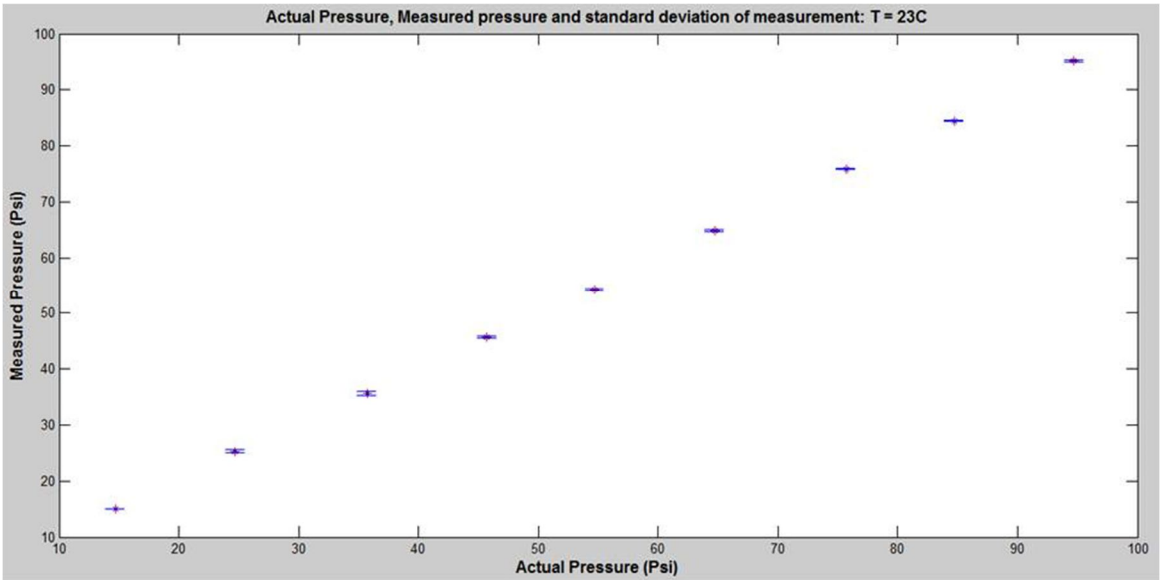

Figure 4.11.2: Actual pressure (psi), measured pressure (psi) & standard deviation of measurement at 23°C.

Similarly, the pressure measurements at 301, 406, 510, and 612°C are demonstrated in the following figures, and are self-explanatory.

Pressure measurement at T=301°C

At 301°C, the measured pressure can be expressed by Equation (4-20).

$$P_{T=301c} = \left(\frac{1}{S_P{}^{(T=301c)}}\right) * [OPD_{After\ TC}{}^{(T=301c)} - C_T{}^{(T=23c)} - dC_{301}] \quad (4\text{-}20)$$

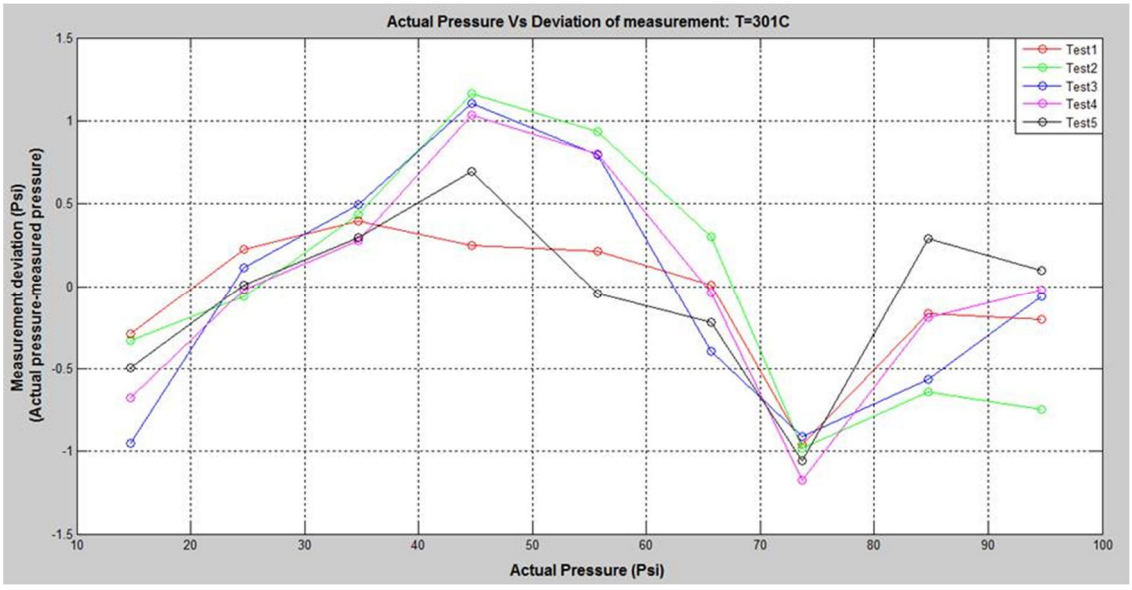

Figure 4.11.3: Actual pressure (psi) vs. measurement error (psi) at 301°C.

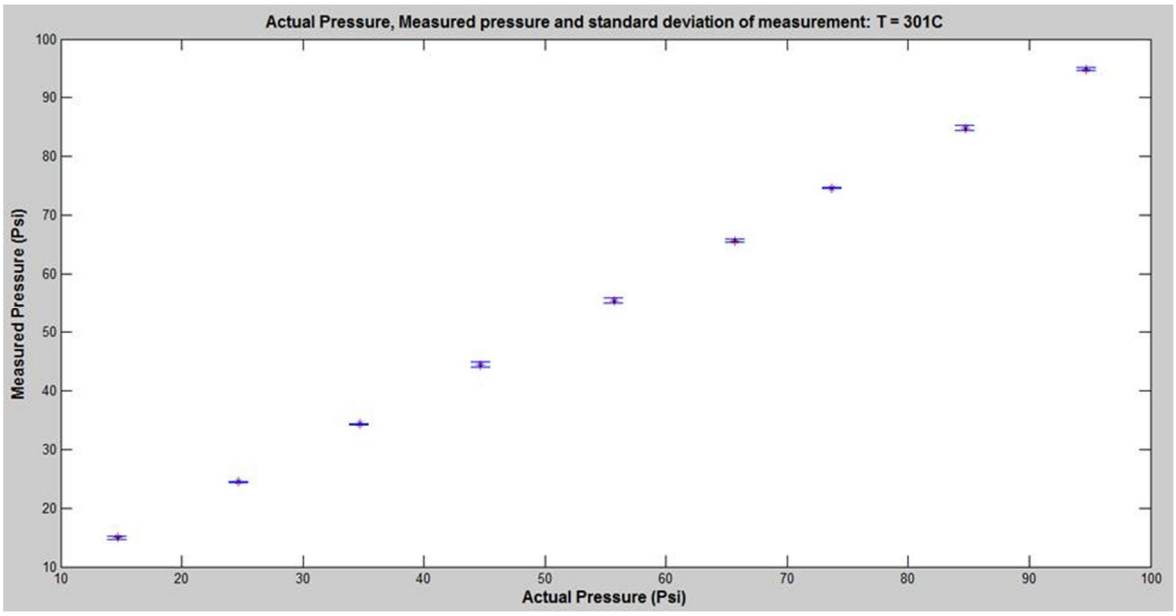

Figure 4.11.4: Actual pressure (psi), measured pressure (psi) & standard deviation of measurement at 301^{o}C.

Pressure measurement at T=406^{o}C

At 406^{o}C, the measured pressure can be written by Equation (4-21).

$$P_{T=406c} = \left(\frac{1}{S_P{}^{(T=406c)}}\right) * [OPD_{After\ TC}{}^{(T=406c)} - C_T{}^{(T=23c)} - dC_{406}] \quad (4\text{-}21)$$

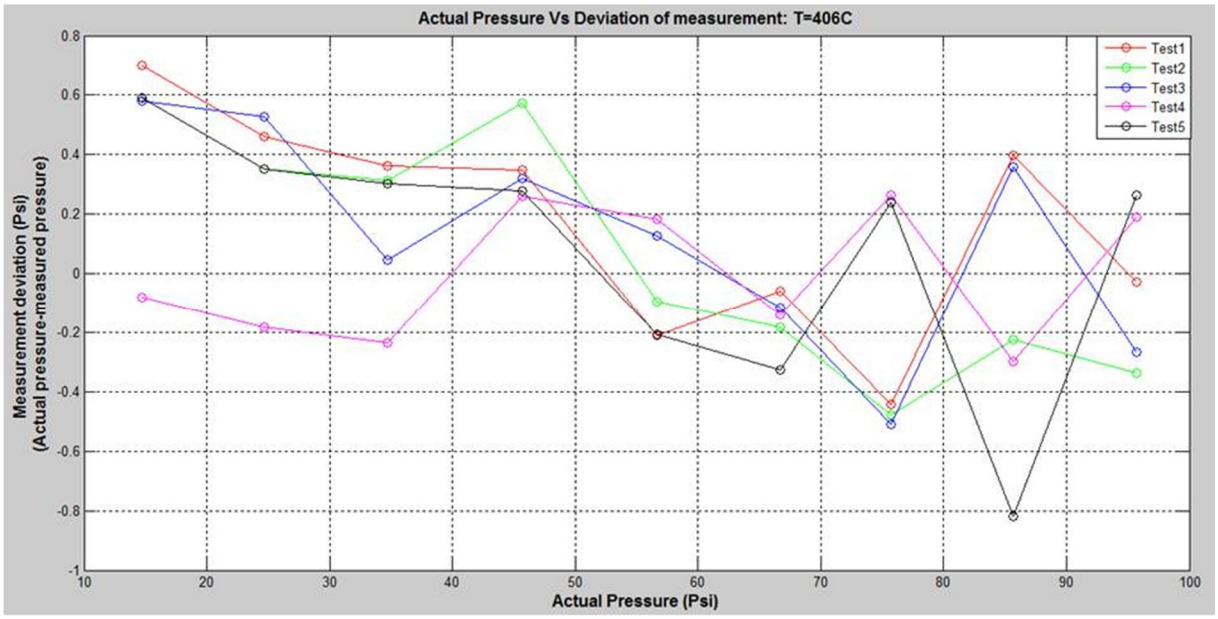

Figure 4.11.5: Actual pressure (psi) vs. measurement error (psi) at 406^{o}C.

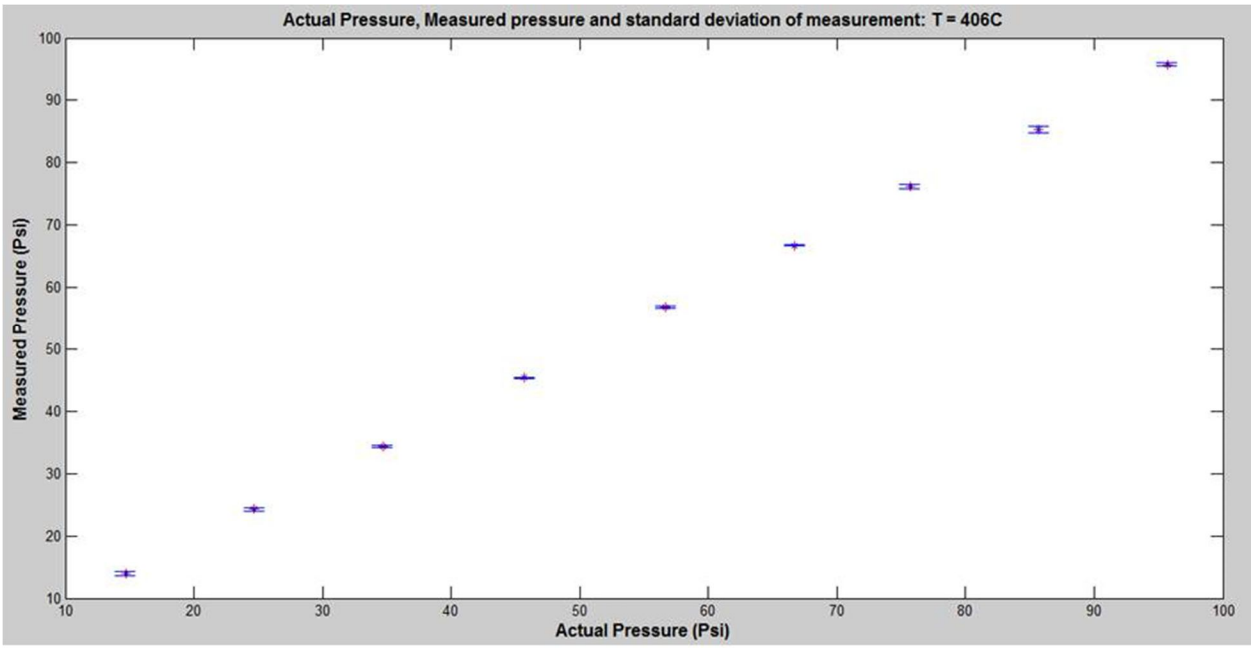

Figure 4.11.6: Actual pressure (psi), measured pressure (psi) & standard deviation of measurement at 406^{o}C.

Pressure measurement at T=510^{o}C

At temperature 510^{o}C, the measured pressure can be expressed by Equation (4-22).

$$P_{T=510c} = \left(\frac{1}{S_P{}^{(T=510c)}}\right) * [OPD_{After\,TC}{}^{(T=510c)} - C_T{}^{(T=23c)} - dC_{510}] \qquad (4\text{-}22)$$

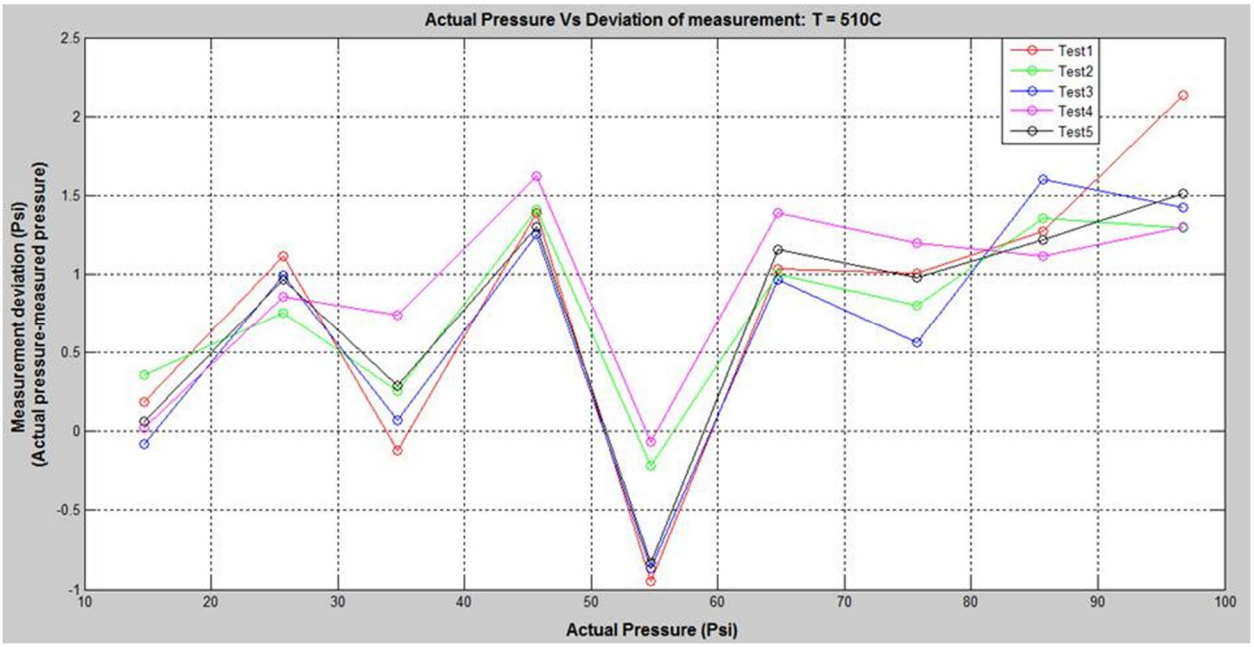

Figure 4.11.7: Actual pressure (psi) vs. measurement error (psi) at 510^{o}C.

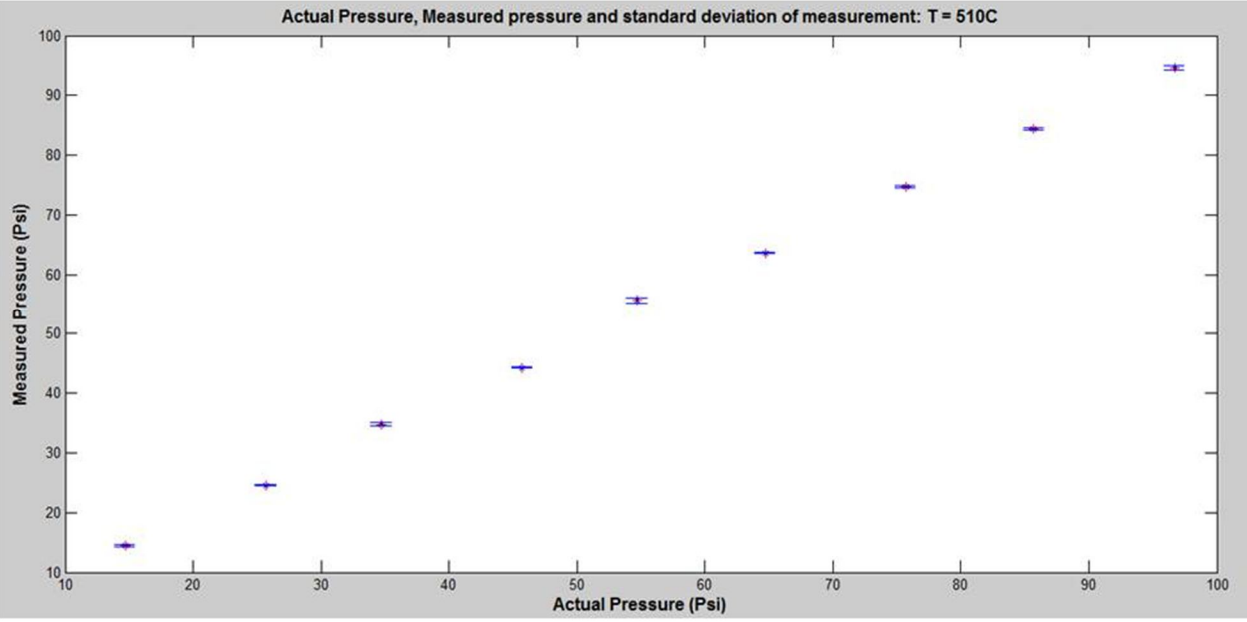

Figure 4.11.8: Actual pressure (psi), measured pressure (psi) & standard deviation of measurement at 510^{o}C.

Pressure measurement at T=612^{o}C

At 612^{o}C, the measured pressure can be written by Equation (4-23).

$$P_{T=612c} = \left(\frac{1}{S_P{}^{(T=612c)}}\right) * [OPD_{After\ TC}{}^{(T=612c)} - C_T{}^{(T=23c)} - dC_{612}] \qquad (4\text{-}23)$$

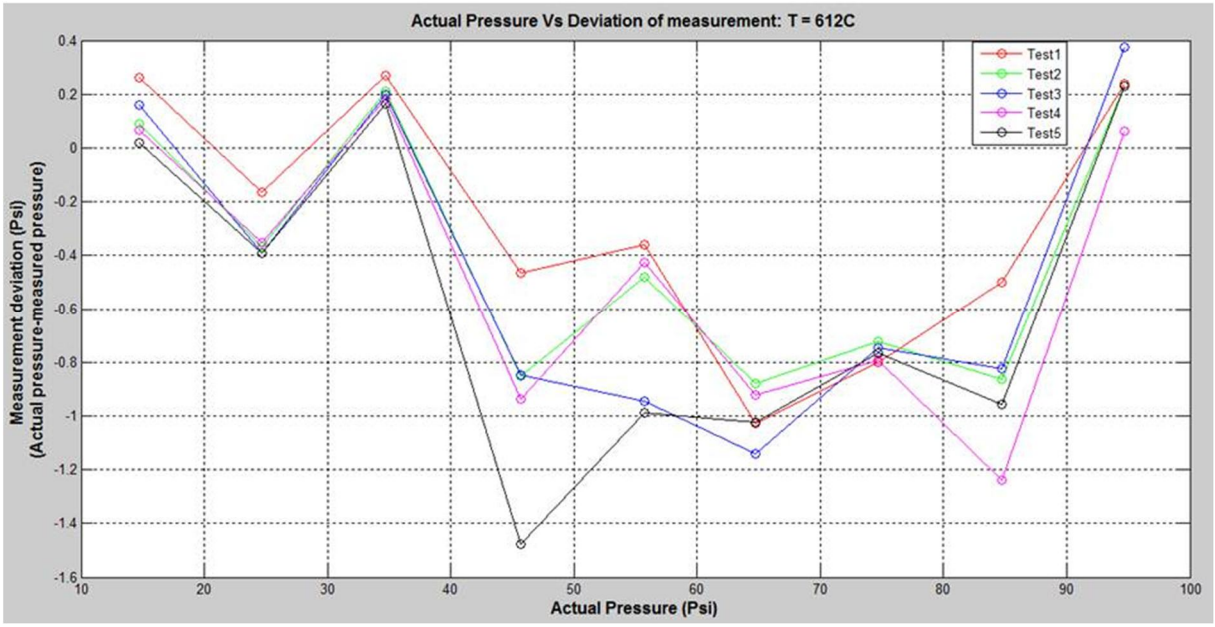

Figure 4.11.9: Actual pressure (psi) vs. measurement error (psi) at 612^{o}C.

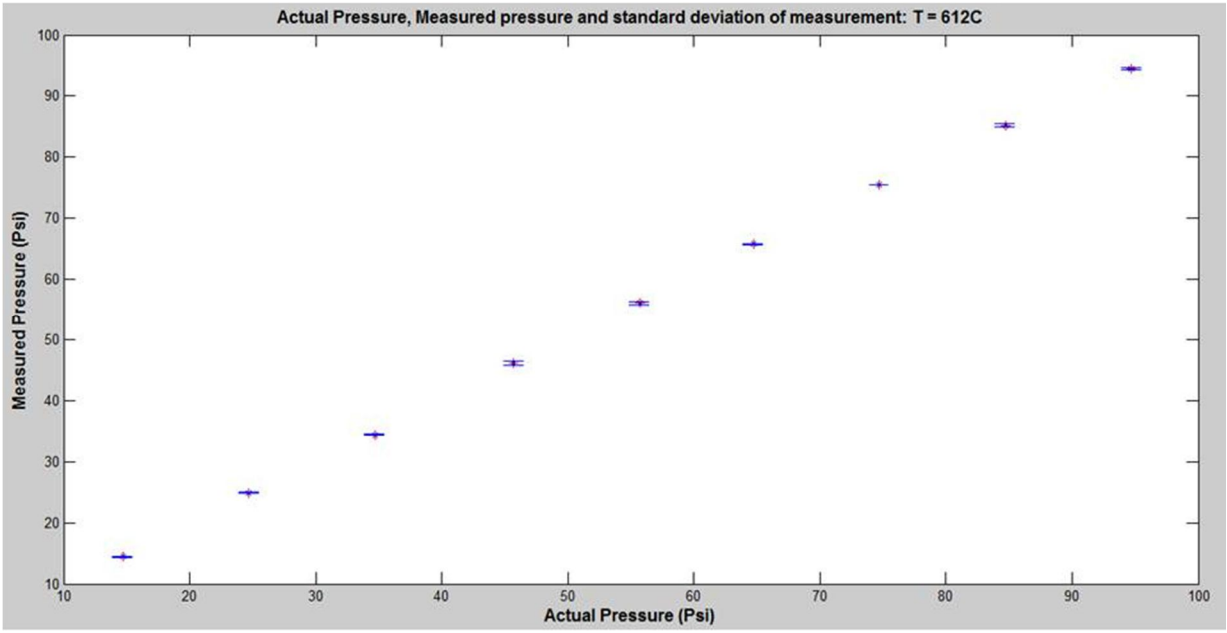

Figure 4.11.10: Actual pressure (psi), measured pressure (psi) & standard deviation of measurement at 612^{o}C.

By analyzing all the pressure measurements by the silica tube cavity (pressure sensor) it can be concluded that the measurement errors are approximately within $\mp 1\ Psi$. Therefore, the pressure sensor can be considered as reasonably accurate. There are several factors that could lead to the small deviation of measurement ($\mp 1\ Psi$). Firstly, the pressure calibration process is not highly accurate. During the pressure calibration, an analog pressure gauge with reasonable pressure range (for better pressure visibility) is used. As a result, it was very difficult to resolve a pressure variation of $\mp 1 \sim 1.5$psi during the pressure calibration process. Secondly, for the silica tube the temperature response is more dominant compared to the pressure response. Therefore, any unseen temperature variation during the pressure calibration process would adversely affect the sensor calibration, and could lead to some deviation of the pressure measurement.

CHAPTER 5: Work summary and future recommendations

5.1 Work summary

The demonstrated composite sensor structure has two cavities; the GIMM fiber cavity and the silica tube cavity. The GIMM fiber cavity is used as a temperature sensor which measures temperature very accurately (errors are within $\mp 0.5^{o}$C). On the other hand, the silica tube responds to both temperature and pressure. Therefore, the temperature data from the GIMM fiber cavity can be used to compensate the temperature response of the silica tube cavity. Finally, the silica tube is demonstrated to work as a pressure sensor at several different temperatures (simultaneous pressure and temperature environment). All the pressure measurements by the silica tube are reasonably accurate, keeping the errors within $\mp$1psi.

5.2 Future work recommendations

The future advancement of this sensor should include the enhancement of sensitivity and accuracy of the pressure measurement. A very thin-walled silica tube could be a good choice. However, this might introduce significant challenges for the splicing between the thin-tube and GIMM fiber. Besides, sensor handling could be substantially challenging due to the increased fragility of the fabricated sensor. Sensible sensor packaging might overcome this problem. Again, the state of the art automatic fusion splicer, and high precision cleaver allow precise control of the quarter pitch length of GIMM fiber. These latest technologies and skilled maneuvering allow longer silica tube cavity length, which could lead to a highly sensitive pressure sensor. Besides, a highly sensitive digital pressure gauge would significantly reduce the pressure calibration error and therefore would diminish the measurement deviation. In addition, if the tube would be highly responsive to pressure but insensitive to temperature, the calibration and modeling of the pressure sensor could be highly simplified. Hence, the pressure measurement by the sensor would be more accurate.

References:

[1] K. T. V. G. and and T. Sun, "Fiber optic sensor technology: an overview," *Sensors and Actuators A: Physical*, vol. 82, pp. 40-61, May 15 2000.

[2] Y. Zhu, K. L. Cooper, G. R. Pickrell, and A. Wang, "High-Temperature Fiber-Tip Pressure Sensor," *JOURNAL OF LIGHTWAVE TECHNOLOGY*, vol. 24, FEBRUARY 2006.

[3] J. Wang, B. Dong, E. Lally, J. Gong, M. H. and, and A. Wang, "Multiplexed high temperature sensing with sapphire fiber air gap-based extrinsic Fabry–Perot interferometers," *OPTICS LETTERS*, vol. 35, March 1 2010

[4] G. Keiser, "Chapter 1: Overview of optical fiber communications," in *Optical Fiber Communications*, ed, 2000, pp. 1.

[5] I. F. M. Mims, "Light-Beam Communications," I. H. W. S. Co, Ed., ed, 1975.

[6] Corning. (2014, June). *"Corning Innovation"*. Available: http://www.corning.com/opticalfiber/innovation/index.aspx

[7] D. Jones, "Introduction to Fiber Optics," N. E. a. T. P. D. a. T. Center, Ed., ed, 1998.

[8] Corning. (June). *"Corning® ClearCurve® Multimode Optical Fiber: Product Information"*. Available: http://www.corning.com/WorkArea/showcontent.aspx?id=36549

[9] G. Keiser, "Chapter 1: Overview of optical fiber communications," in *Optical Fiber Communications*, 3rd ed, 2000, pp. 12.

[10] G. Keiser, "Chapter 3: Signal degradation in optical fibers," in *Optical fiber communications*, 3rd ed, 2000, pp. 97.

[11] G. Keiser, "Chapter 2: Optical fibers: Structures, waveguiding, and fabrication," in *Optical fiber communications*, 3rd ed, 2000, pp. 34-37.

[12] G. Keiser, "Chapter 2: Optical fibers: Structures, waveguiding, and fabrication," in *Optical Fiber Communications*, ed, 2000, pp. 40-41.

[13] G. Keiser, "Chapter 2: Optical fibers: Structures, waveguiding, and fabrication," in *Optical Fiber Communications*, ed, 2000, pp. 46.

[14] G. Keiser, "Chapter 2: Optical fibers: structures, waveguiding, and fabrication," in *Optical fiber communication*, 3rd ed, 2000, pp. 55.

[15] E. Udd, "An overview of fiber-optic sensors," *Rev. Sci. Instrum.*, vol. 66 (6), August 1995 1994.

[16] B.D.Gupta, "Chapter 1: Optical fiber sensors," in *Fiber optic sensors: Principles and applications*, 2nd ed, 2006, pp. 2-5.

[17] J. Castrellon-Uribe. (2012, june). "*Optical Fiber Sensors: An Overview"*. Available: http://www.intechopen.com/books/fiber-opticsensors/optical-fiber-sensors-an-overview

[18] K. Fidanboylu and H. S. Efendioğlu, "FIBER OPTIC SENSORS AND THEIR APPLICATIONS," in *5th International Advanced Technologies Symposium (IAT S'09)*, Karabuk, Turkey 2009.

[19] Juncheng Xu, Xingwei Wang, Kristie L Cooper, G. R. P. and, and A. Wang, "Miniature fiber optic pressure and temperature sensors," in *Fiber Optic Sensor Technology and Applications IV, Proc. of SPIE* 2005.

[20] C. Ma, N. Wang, E. M. Lally, and A. Wang, "Intrinsic Fabry-Pérot Interferometric (IFPI) fiber pressure sensor," in *Proc. of SPIE*, 2010.

[21] M. Yu, "Fiber Optic Sensor Technology" [Online]. Available: https://sem.org/PDF/fiber_optic_sensor_technology.pdf

[22] N. Lagakos, J. H. C. and, and J. A. Bucaro, "Microbend sensors," *Appl. Opt.*, vol. 26, pp. 2171-2180, 1987.

[23] F. Shen, "UV-Induced Intrinsic Fabry-Perot Interferometric Fiber Sensors and Their Multiplexing for Quasi-Distributed Temperature and Strain Sensing," Ph.D. dissertation, ECE, Virginia Polytechnic Institute and State University, Blacksburg, 2006.

[24] X. Chen, F. Shen, Z. Wang, Z. H. and, and A. Wang, "Micro-air-gap based intrinsic Fabry–Perot interferometric fiber-optic sensor," *APPLIED OPTICS*, vol. 45, 20 October 2006.
[25] Z. Huang, "Quasi-Distributed Intrinsic Fabry-Perot Interferometric Fiber Sensor for Temperature and Strain Sensing " Ph.D. dissertation, ECE, Virginia Polytechnic Institute and State University, Blacksburg, 2006.
[26] P. Hariharan, "Volume II, CHAPTER 21: INTERFEROMETERS," in *IVPV handbook of optics*, ed, pp. 21.2-21.7.
[27] Y. Zhu, "Chapter 3: Ultra Miniature Fiber-Tip Pressure Sensor," Ph.D. dissertation, ECE, Virginia Polytechnic Institute and State University, Blacksburg, VA, 2007.
[28] S. Guo, H. Eriksen, K. Childress, A. Fink, and M. Hoffman, "HIGH TEMPERATURE HIGH ACCURACY PIEZORESISTIVE PRESSURE SENSOR BASED ON SMART-CUT SOI," in *MEMS*, Tucson,AZ, USA, 2008.
[29] A. D. Kurtz, A. A. Ned, S. Goodman, and A. H. Epstein, "Latest Ruggedized High Temperature Piezoresistive Transducers," presented at the NASA 2003 Propulsion Measurement Sensor Development Workshop, Huntsville, Alabama, US, 2003.
[30] A. D. Kurtz, A. A. Ned, and A. H. Epstein2, "Ultra High Temperature, Miniature, SOI Sensors for Extreme Environments, " presented at the IMAPS International HiTEC 2004 Conference Santa Fe, New Mexico, US, 2004.
[31] R. S. Okojie, A. A. Ned, and A. D. Kurtz, "Operation of alpha(GH)-SiC pressure sensor at 500 degrees C," *Sensors and Actuators a-Physical*, vol. 66, pp. 200-204, 1998.
[32] X. Wang, J. Xu, Y. Zhu, B. Yu, M. Han, Z. Wang, *et al.*, "Verifying an all fused silica miniature optical fiber tip pressure sensor performance with turbine engine field test," in *Proc. of SPIE*
[33] C. Wu, H. Y. Fu, K. K. Qureshi, B.-O. Guan, and H. Y. Tam, "High-pressure and high-temperature characteristics of a Fabry–Perot interferometer based on photonic crystal fiber," *OPTICS LETTERS*, vol. 36, February 1 2011.
[34] M. Li and Q. a. Wang, "Miniature high sensitivity diaphragm-based optical fiber Fabry-Perot pressure sensor, " in *International Conference on Electronics, Communications and Control (ICECC)*, Zhejiang, 2011 pp. 328 - 330.
[35] J. Xu, "High temperature high bandwidth fiber optic pressure sensors," Ph.D. dissertation, ECE, Virginia polytechnique institute and state university, Blacksburg, VA, USA, 2005
[36] N. S1, Y. M, Z. X, and H. AH, "Miniature fiber optic pressure sensor with composite polymer-metal diaphragm for intradiscal pressure measurements," *J Biomed Opt*, vol. 13, Jul-Aug 2008.
[37] X. Chen, "Fiber Optic Pressure Sensor Fabrication Using MEMS Technology," Master's thesis, ECE, Virginia polytechnique institute and state university, Blacksburg, VA, USA, 2003.
[38] Y. Zhu, "Chapter 2: Miniature Fiber-Optic Sensors for High-Temperature Harsh Environments," Ph.D. dissertation, ECE, Virginia Polytechnic Institute and State University, Blacksburg, Virginia, 2007
[39] X. Chen, F. Shen, A. Wang, Z. Wang, and Y. Zhang, "Novel Fabry-Perot fiber optic sensor with multiple applications," in *Proc. of SPIE* Bellingham, WA, 2004.
[40] U. UNIVERSITET, "Fresnel's equation for reflection and refraction" [Online]. Available: http://www.teknik.uu.se/ftf/education/ftf2/Optics_FresnelsEqns.pdf
[41] R. Wayne, "Chapter 2: The geometric relationship between object an image," in *Light and video microscopy*, 2nd ed, 2014, pp. 35.
[42] F. a. Shen and A. Wang, "Frequency-estimation-based signal-processing algorithm for white-light optical fiber Fabry-Perot interferometers," *Appl. Opt. 44*, pp. 5206-5214, 2005.
[43] B. Qi, G. R. Pickrell, J. Xu, P. Zhang, Y. Duan, W. Peng, *et al.*, "Novel data processing techniques for dispersive white light interferometer," *Opt. Eng.*, pp. 3165-3171, 2003.
[44] M. Han, Y. Zhang, F. Shen, G. R. a. Pickrell, and W. A., "Signal-processing algorithm for white-light optical fiber extrinsic Fabry-Perot interferometric sensors," *Opt. Lett.*, pp. 1736-1738, 2004.
[45] J. Deng, H. Xiao, and W. Huo, "Optical fiber sensor-based detection of partial discharges in power transformers," *Optics and Laser Technology*, vol. 33, pp. 305-311, 2001.

[46] J. Xu, G. Piekrell, and a. B. Yu, "Epoxy-free high temperature fiber optic pressure sensors for gas turbine engine applications," in *Proc. Sensors for Harsh Environments*, Philadelphia, 2004, pp. 1-10.
[47] Y. Zhu and a. A. Wang, "Miniature Fiber-Optic Pressure Sensor," *IEEE PHOTONICS TECHNOLOGY LETTERS*, vol. 17, FEBRUARY 2005.
[48] X. Wang, J. Xu, Y. Zhu, K. L. Cooper, and a. A. Wang, "All-fused-silica miniature optical fiber tip pressure sensor," *OPTICS LETTERS*, vol. 31, April 1, 2006 / Vol. 31, No. 7 / OPTICS LETTERS 2006.
[49] E. Cibula and a. D. Donlagić, "Miniature fiber-optic pressure sensor with a polymer diaphragm," *Appl. Opt*, pp. 2736–2744 2005.
[50] E. Cibula, D. Donlagic, and a. C. Stropnik, "Miniature Fiber Optic Pressure Sensor for Medical Applications," in *Proceedings of IEEE Sensors* Orlando, FL, 2002, pp. 711–714.
[51] X. Chen, F. Shen, Z. Wang, Z. Huang, and a. A. Wang, "Micro-air-gap based intrinsic Fabry–Perot interferometric fiber-optic sensor," *APPLIED OPTICS*, vol. 45, 20 October 2006.
[52] C. Ma, B. Dong, E. M. Lally, and a. A. Wang, "Optimization of Single-/Multi-/Single-Mode Intrinsic Fabry–Perot Fiber Sensors," *JOURNAL OF LIGHTWAVE TECHNOLOGY*, vol. 30, JULY 15 2012.
[53] A. Wang and G. Pickrell, "Multiplexed Optical Fiber Sensors for Coal Fired Advanced Fossil Energy Systems," Virginia polytechnique institute and state university, http://www.osti.gov/scitech/December 2011.
[54] "P. technologies. Appendix: quartz/silica characteristics" [Online]. Available: http://issuu.com/molex/docs/polymicro-technolgies/69?e=1375594/3758752
[55] E. J. Hearn, "Thick cylinders," in *Mechanics of materials*, 3rd ed, 1997, pp. 219-222.
[56] B. Qi, G. Pickrell, P. Zhang, Y. Duan, W. Peng, J. Xu, *et al.*, "Fiber Optic Pressure and Temperature Sensors for Oil Down Hole Application," in *Fiber Optic Sensor Technology and Applications, 182 Proceedings of SPIE*, 2001.
[57] X. Wang, "Optical Fiber Tip Pressure Sensor," ECE, Virginia polytechnique institute and state university, Master's thesis, 2004.
[58] R. G. Ball, "The Gaseous State," in *CHEMISTRY principles and practice*, ed, 2009, pp. 219.

APPENDIX: A

Temperature coefficients & constant (for GIMMF) [Equation (4-4)]	
GF_5 =	1.7520E-03
GF_4 =	-1.3555E+01
GF_3 =	4.1948E+04
GF_2 =	-6.4908E+07
GF_1 =	5.0217E+10
GF_0 =	-1.5541E+13

Temperature coefficients & constant (for silica tube) [Equation (4-7)]	
ST_{T5}	-7.0191E-15
ST_{T4}	1.2485E-11
ST_{T3}	-1.0118E-08
ST_{T2}	4.7376E-06
ST_{T1}	5.6347E-04
ST_{T0}	-3.3565E+03

Temperature dependent coefficients & constant (for silica tube) [Equation (4-7)]	
$C_T^{(T=23c)}$	2.6874E+03
dC_{301}	-6.5901E-04
dC_{406}	-1.1564E-03
dC_{510}	-6.0617E-04
dC_{612}	1.7821E-03

Temperature dependent pressure sensitivity [um/psi] (for silica tube)	
$S_P^{(T=23c)}$	-2.7516E-04
$S_P^{(T=301c)}$	-2.3282E-04
$S_P^{(T=406c)}$	-2.0129E-04
$S_P^{(T=510c)}$	2.3999E-04
$S_P^{(T=612c)}$	-4.0548E-04